Louisiana State University
LSU Digital Commons

LSU Master's Theses Graduate School

2013

Spectral breast CT : effect of adaptive filtration on CT numbers, CT noise, and CT dose

Justin Silkwood
Louisiana State University and Agricultural and Mechanical College

Follow this and additional works at: https://digitalcommons.lsu.edu/gradschool_theses

Part of the Physical Sciences and Mathematics Commons

Recommended Citation
Silkwood, Justin, "Spectral breast CT : effect of adaptive filtration on CT numbers, CT noise, and CT dose" (2013). *LSU Master's Theses*. 1332.
https://digitalcommons.lsu.edu/gradschool_theses/1332

This Thesis is brought to you for free and open access by the Graduate School at LSU Digital Commons. It has been accepted for inclusion in LSU Master's Theses by an authorized graduate school editor of LSU Digital Commons. For more information, please contact gradetd@lsu.edu.

SPECTRAL BREAST CT: EFFECT OF ADAPTIVE FILTRATION ON CT NUMBERS, CT NOISE, AND CT DOSE

A Thesis

Submitted to the Graduate faculty of the
Louisiana State University
Agricultural and Mechanical College
In Partial Fulfillment of the
Requirements for the Degree of
Master of Science

in

The Department of Physics and Astronomy

by
Justin Silkwood
B.S., Southwestern Oklahoma State University, 2010
May 2013

ACKNOWLEDGEMENTS

First and foremost, I thank my advisor Dr. Polad Shikhaliev for providing guidance throughout my entire research experience. Thank you very much for remaining patient during headache inducing moments; it really meant a lot. Next, I thank my wife Candace for all she has done for me during my time in graduate school. Appreciation is also extended to the members of my committee: Dr. Newhauser, Dr. Matthews, and Dr. Deibel. Their input and helpful comments during the preparation of this thesis were of great help. Lastly, I express my appreciation to my family and friends for being there for me during this work.

TABLE OF CONTENTS

ABSTRACT

Purpose: Adaptive filtration facilitates spectral breast CT by decreasing count rate and dynamic range requirements to photon counting detectors. This project investigated the effect of adaptive filtration on beam hardening, CT numbers, noise, and dose in dedicated breast CT.

Methods: Adaptive filters were simulated to provide a flat fluence at the detector surface when used with a 14 cm breast phantom at 120 kVp. Beam hardening with each filter type was measured against increasing x-ray beam half-fan angle. Breast CT images were simulated with and without an adaptive filter in the beam at multiple tube voltages. CT number, noise, and contrast to noise ratio (CNR) were measured for contrast elements inside the phantom.

Finally, dose measurements were performed with and without an adaptive filter to determine its effect on breast dose.

Results: Acrylic filters, while larger in size, provided a more uniform spectral distribution across the detector field of view compared to other filters tested.

Without the adaptive filter in the beam, CT numbers, noise and CNR of the contrast elements were non-uniform across the CT images, and became uniform when the adaptive filter was used. When combining an adaptive filter and scaled x-ray exposure, the CNR increased and became comparable to or higher than the CNR without using an adaptive filter.

Measurements showed breast dose distributions were more spatially uniform with an adaptive filter than without. Furthermore, the dose distribution across the phantom with the adaptive filter was more uniform at lower tube voltages than at higher tube voltages.

Conclusion: We concluded that the filter material should be similar to breast tissue with respect to the effective atomic numbers and density. Acrylic adaptive filters provided the flattest intensity with minimal beam hardening for the 14 cm breast phantom. Finally, breast dose uniformity with filter was comparable or better than without filter.

CHAPTER 1. INTRODUCTION

1.1. Breast cancer detection

Breast abnormalities typically present as macrocalcifications, microcalcifications, solid masses, cystic liquid-filled masses, or a combination of these above characteristics [1, 2]. Many techniques exist to identify and differentiate these abnormalities including the breast self-examination, physical examination by a trained physician, mammography, ultrasound, and breast MRI.

Mammography has been the primary screening tool for breast cancer for more than forty years [3-8]. The procedure is widely known and publically accepted. A typical screening mammography procedure requires less than twenty minutes and is less costly than other procedures like breast MRI or ultrasound. Screening mammography has a relatively low risk for inducing radiogenic cancer incidence because of the low doses delivered [5, 9, 10]. An average sized breast receives an average glandular dose of around 4.4 mGy from two-view screening mammography [5, 10-12]. Although the current gold standard, mammography has limitations. One problem is the appearance of overlapping tissues; normal tissue in front of or behind a small cancer may obscure the cancer's observation on a mammogram. Normal structures inside the breast may also look suspicious when viewed in projection. Two views are taken at nearly orthogonal angles to read around these effects, but this approach does not actually fix the problem in either image [3-5, 7, 10]. Instead, if screening mammography results are positive for suspicious structures, advanced diagnostic tools are utilized like breast MRI, ultrasound of the breast, a diagnostic mammogram, and biopsy of the suspected area(s). Breast MRI provides an advantage over mammography in that it produces tomographic slices with high resolution [2, 4, 5, 10]. However, MRI is expensive [3], time consuming to perform, and routinely uses contrast agent [4, 5, 7, 13]. Also, MRI cannot image microcalcifications due to an inherent lack of a contrast detection mechanism for calcium. Ultrasound can quickly determine if a suspicious mass is solid or fluid-filled: solid masses could be an indicator for cancer, whereas fluid-filled masses typically indicate a benign cyst [1, 2, 4, 7, 9]. However, ultrasound image quality is poor compared to other imaging methods. A diagnostic mammogram provides higher-quality magnified views of areas containing suspicious masses compared to a screening mammogram, but with a greater radiation dose to the breast. A biopsy is the definitive method to determine whether or not a suspicious mass is cancerous. However, if an imaging modality clearly indicates a mass is benign, then biopsy can be avoided [1, 2, 14].

1.2. History of breast CT

CT imaging was first introduced to the clinic around 1973 [15], and it was quickly assessed for breast imaging. Traditional whole thorax CT was determined to be unacceptable for breast cancer screening for a number of reasons. Due to long acquisition times, breathing artifacts blurred the reconstructed images so that detecting small cancers, especially those not observable using traditional mammography, would be difficult. Using traditional CT to obtain breast CT images also resulted in unnecessary dose by placing critical organs in the thorax in the path of the beam. A new geometry of CT scanner for dedicated breast CT was proposed in 1976 to address the concerns outlined above [16]. Chang *et al*. utilized a prototype scanner called the GE Computed Tomographic Breast Scanner (CT/M) to scan 1,625 patients over nearly three years [17]. The scanner was laid on its side as compared to a traditional CT scanner; the tube and detection equipment rotated on a horizontal plane around the breast and obtained coronal slice tomographic images of the breast (Figure 1). The patient was positioned initially on an upright tabletop, and then lowered into scanning position. The breast was immersed in body temperature circulating water within the gantry; the water equalized the x-ray fluence to accommodate detector count-rate limitations. The gantry stepped vertically to scan each slice while the patient remained stationary. A scan time of 10 seconds for each slice increased the risk of motion artifacts [8, 10] and the reconstruction time was 90 seconds per slice. CT number values ranged from -127 HU to +128 HU. The total dose to each breast was kept around 1.75 mGy for the entire procedure.

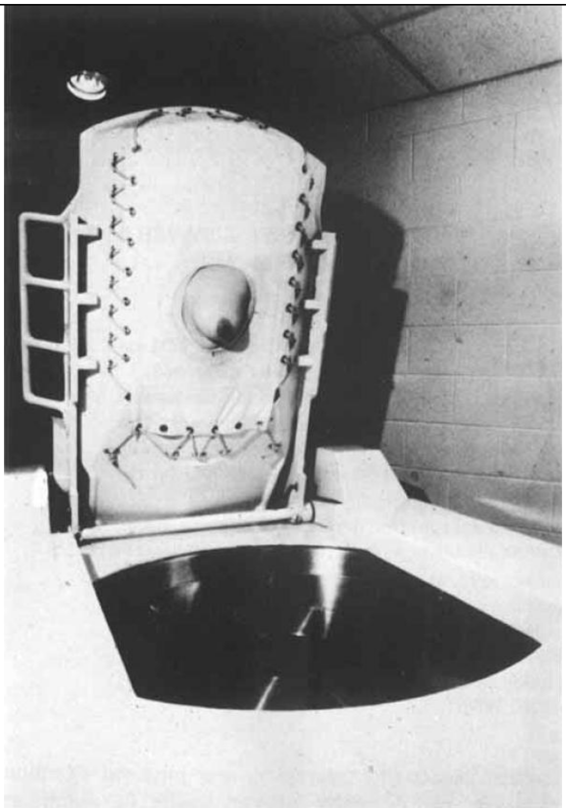

Figure 1. The GE CT/M scanner is shown with a patient placed on the couch top in the vertical position. The patient is lowered into a horizontal position with the breast placed in a water bath within the gantry. (Used with permission from [17].)

Each breast was imaged twice: once to obtain a baseline reading, and again after injection of iodine contrast medium. Most breast cancers preferentially take up contrast medium compared to normal structures in the breast. This higher concentration of iodine contrast changes the CT number, recorded in Hounsfield units (defined in section 2.3.2), of breast cancer more than that for normal tissue. This change in CT number between the scans was what was used to identify abnormalities. The scanner had a slice thickness of 10 mm and a pixel size of 1.56 x 1.56 mm^2 [16]; this large slice thickness and pixel size prevented small lesions from being resolved. Also, larger lesions could be missed if they fell along the border between two slices due to volume averaging effects [17].

In addition to receiving a breast CT, each patient also had a physical examination and a two-view mammogram. Out of 1625 patients, 78 cancers of the breast were discovered by at least one of these means and were histologically proven. The cancers' maximum diameter ranged from 2 mm to 9 cm. Of the 78 cancers diagnosed, the CT/M system detected 73, resulting in a detection efficiency of 94% for the study. Traditional mammography detected 60 of the 78 cancers present, for a detection efficiency of 77%. Physical examination's detection rate was 64% during this study. The authors concluded that this scanner could be an attractive tool for screening the breasts of premenopausal women for whom the breasts were typically denser and harder to achieve proper contrast resolution using two-view mammography. The same advantage was also expected for screening the breasts of women who were at a higher risk for breast cancer due to a family history of breast cancer or who were genetically predisposed to breast cancer. However, this device was infeasible as a screening tool for the general population due to the prohibitive cost of the procedure in comparison to traditional mammography, the length of the procedure, and the mandatory use of contrast medium, which can cause adverse reactions in approximately 3.4% of the population [8, 17]. Ultimately, breast CT development was abandoned until around 2001.

Boone [10] and Ning [8] independently proposed dedicated breast CT scanners that utilized flat-panel detectors (Figure 2). The scanning geometry was much the same as with the CT/M scanner introduced by Chang [7, 8, 10, 17].

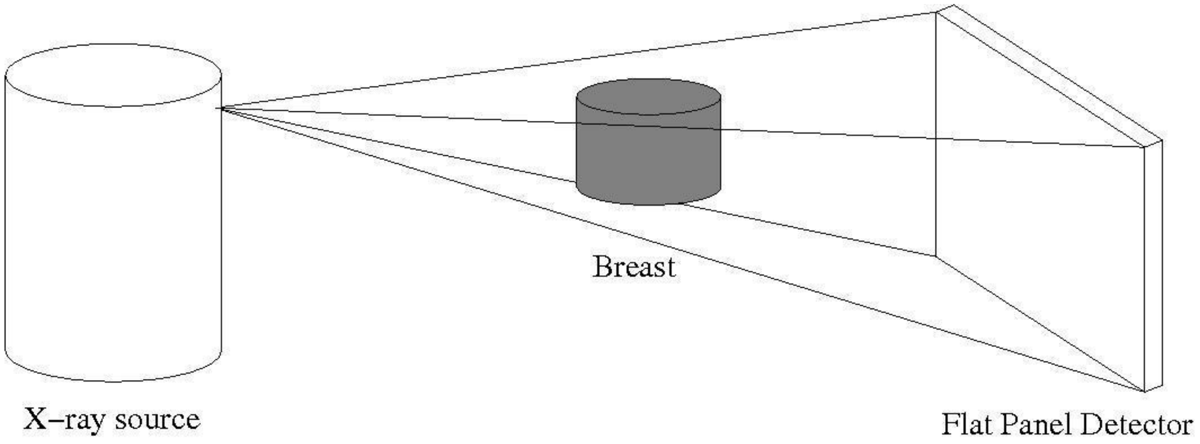

Figure 2. Concept for a breast CT scanner using cone-beam geometry. The x-ray source emits an open geometry beam. The breast hangs pendant in the beam, and the flat-panel detector intercepts the primary beam and scatter. The Chang's [16,17] breast CT system used high-pressure xenon gas detectors, while later systems used flat-panel detectors.

However, Chang's [16, 17] fan-beam geometry was replaced with a cone beam geometry. The patient was once again imaged prone with the breast in pendant geometry [7, 8, 10]. The bucket of water was removed in favor of a beam compensating filter that modified the photon fluence to account for decreasing breast thickness moving from the chest wall towards the nipple [8]. The scanner proposed by Boone [10] was constrained to deliver no higher dose than that received during typical two-view mammography. For breasts with compressed thickness at or greater than 5 cm, the average glandular dose deposited by the CT procedure was lower than two view mammography. The average glandular dose for breasts with compressed thickness below 5 cm was found to be not much greater than that for two-view mammography [10]. Boone [10] suggested that breast CT will provide more homogeneous dose to the breast than mammography. He further proposed that if the linear non-threshold cancer risk model for radiation dose holds true, then mammography and dedicated breast CT pose about the same radiation risk per procedure to the patient. However, if the risk model is non-linear in nature, then the more homogeneous dose delivered by dedicated breast CT provides a net benefit over mammography in terms of overall radiation risk. This applies even though the average glandular dose to the breast is similar for both breast CT and mammography. Initially, Boone simulated a flat panel detector using Monte Carlo code and took scans of a cadaver breast with a traditional CT scanner to gather data [10]. However, once the feasibility of a dedicated breast CT to deliver scans with acceptable quality and with limited dose was proven, he built a prototype flat panel scanner [7].

In 2006, Boone [7] published an updated paper detailing his work with a prototype breast CT scanner [7]. The scanner obtained a full 360 degree acquisition in 16 seconds with a flat-panel detector. Scan parameters were selected so that the same or lower average glandular dose to the breast was achieved using the breast CT as with two-view mammography. Fifty-five women were imaged; 10 were healthy volunteers for a Phase 1 trial, while the other 45 women scanned for a Phase 2 trial had an increased risk of developing breast cancer. The scanner reconstructed 300 slices; each slice was a 512x512 image matrix with 0.194x0.194 mm^2 pixels. This study concentrated on imaging without using contrast agents.

Independently, Ning performed theoretical research outlining the improvements that could be realized from utilizing a flat-panel detector in a dedicated breast CT unit [8]. His proposed system could provide improvements in contrast resolution, detectability of small cancers, and lesion localization compared to two-view mammography. For a typical exam, doses of 3.36 mGy and 2.35 mGy were expected in 12 cm and 10 cm diameter breasts, respectively. These dose levels were similar to that observed for traditional mammography when comparing dose to similarly sized breasts.

A major challenge for using a flat-panel detector is ensuring the scatter to primary ratio (SPR) is low enough to provide acceptable image quality. Ning found that an SPR of 15% or lower would provide acceptable image quality and cupping artifact. (For a description of cupping artifacts, see Appendix A.) Using an effective energy of 38 keV, Ning was able to visualize 1 mm diameter carcinomas and calcifications only a few hundred micrometers thick [8]. Quantitative investigations have shown that detected scatter remains one of the major problems for cone beam breast CT [3, 5, 11, 18-20]. The open geometry of the x-ray beam creates a substantial amount of scatter in the breast and this scatter arrives at the detector. Using a scatter rejecting grid is not appropriate for flat panel detectors because grids create Moire artifacts when used with a pixelated detector [21]. Another major problem of cone beam breast CT is the electronic noise inherent in flat panel detectors [5, 22, 23]. Scatter and detector noise together result in substantial deterioration of contrast to noise ratio (CNR) in cone beam breast CT.

1.3. Photon counting spectral CT

Photon counting spectral computed tomography (PCSCT) has a number of advantages compared to conventional CT with energy integrating detectors. These advantages include rejection of electronics noise, improved signal to noise ratio with photon energy weighting, material decomposition in a single CT scan, and substantial decrease in patient dose. In the last decade, PCSCT has been investigated in a variety of aspects. These investigations were primarily focused on photon counting detector developments [24-27], optimal use of energy selective data to achieve a highest possible CNR [11, 28-30], detector count rate and image artifact problems [31-33], material decomposition [11, 34-38], and material-selective PCSCT imaging with experimental prototypes [39-43]. Recently, direct experimental comparison of PCSCT to a clinical CT system (Siemens Sensation 16) was reported for breast imaging. The PCSCT system showed a similar CNR compared to the clinical CT system while providing a clear advantage of material decomposition with a single CT scan and fixed tube voltage [42]. Photon Counting breast CT itself was first proposed in [29], and further investigated in other works [11, 42]. Photon counting breast CT has now gained considerable interest, and additional groups are investigating it [44].

In 2008, Shikhaliev published a feasibility study outlining the possible benefits of using a photon counting energy resolving detector for breast CT [11], using a cadmium zinc telluride (CZT) detector. The photon counting capability of the CZT detector allowed each photon to be independently detected and assigned to a specific energy bin. Energy weighting was applied during post processing of the image. In his work, photon counting, charge integrating and photon energy weighting images were simulated. The simulation used a 90 kVp tube operating potential, a tungsten tube anode, and 2 mm Al filtration with 660 mR entrance skin exposure, which corresponds to approximately 4.4 mGy average glandular dose to a 14 cm diameter breast comprised of 50/50 adipose/glandular tissue, similar to the average dose to a breast of this size using traditional two-view mammography. CNR improvement through energy weighting was quantified, with the CNR of carcinoma, blood, adipose tissue, iodine and $CaCO_3$ improved by factors of 1.16, 1.20, 1.21, 1.36, and 1.35 respectively. Dual energy subtraction was simulated for $CaCO_3$ and iodine. Energy weighting was applied before material decomposition was performed. The CNR of $CaCO_3$ and iodine improved by factors of 1.35 and 1.33, respectively, when material decomposition was performed on the 50/50 adipose/glandular background.

Helical scanning of a single row of detectors provided scatter rejection and limited wasted dose to the breast. However, this setup was not practical in a clinical system because the scan time would be too long. Instead, Shikhaliev suggested a multi-slit, multi-slice (MSMS) scanning approach (Figure 3) [11]. MSMS works by having several rows of detectors spaced apart from each other. The scanner rotates helically about the z-axis and translates along the z-axis by the same distance as the spacing between the detector rows. A cone beam is collimated into separate fan beams with a thickness of 0.2 mm-1.5 mm by a fore collimator. The fan beams then pass through the breast tissue. The beam exits through an aft collimator that intercepts much of the scatter produced in the patient. This method provides the benefit of a short scan time with the scatter rejection benefits of using fan beams. Reducing the SPR of a beam incident on a detector is important for maintaining high CNR. A 50% SPR associated with cone beam geometry reduces CNR by 32%. Using thin, collimated beams theoretically reduces SPR to less than 7% for MSMS. Therefore, utilizing MSMS geometry alone could improve CNR by a factor of 1.47 [11]. The 2-row photon counting CZT detectors that are currently commercially available are well suited to the MSMS geometry.

Experimental results with a CZT detector based system were reported in [36] and [42]. Using the beam stop method, SPR was measured to be 2.3% for the photon counting spectral detector [36]. The photon counting spectral scanner was deemed feasible for CT imaging and added the benefits of photon counting, energy weighting, scatter rejection and single scan dual energy subtraction when compared to CT scanners with flat panel and conventional detectors [36, 42]. The detector used in [42] was constructed from 16 CZT crystals measuring 3 mm thick by 16 mm wide by 4.7 mm tall. A 3 mm thick CZT crystal absorbs 99% of the incident flux from a 120 kVp beam that has passed through 10 cm of acrylic, which approximates breast tissue. However, around 15% of the intercepted photons are below the minimum energy detection threshold.

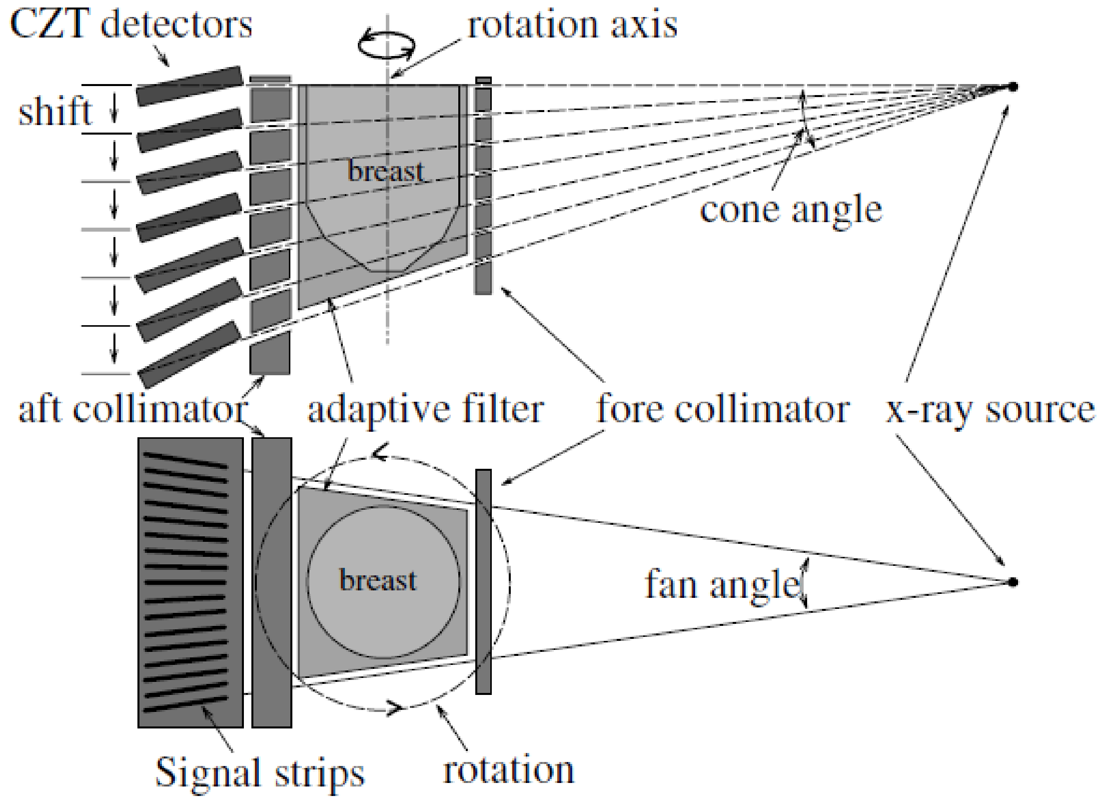

Figure 3. Multi-slit, multi-slice proposed design [11]. The scanner rotates about the rotation-axis while translating along the z-axis. The cone beam is collimated into multiple fan beams.

Each crystal module, shown in Figure 4, was further divided on the anode into a pixel array measuring 2 rows by 16 columns. A voltage of -600 V was applied to the cathode, with the cathode facing the incoming x-ray flux. Most of the x-ray photons interact within a shallow depth inside the crystal, so using the cathode as the entrance face helps to remove holes, or vacancies created in the crystal from ejected electrons. Each pixel measured 1.0 x 1.0 mm^2. Sixteen crystal modules were placed flush with each other to give a field of view width of 25.6 cm and height of 2 mm at the detector plane. The source to image distance for the spectral CT system was 85 cm, and the source to isocenter distance was 53 cm. Thus, the effective field of view at isocenter was 15.9 cm wide, and the effective pixel dimensions were 0.62 x 0.62 mm^2.

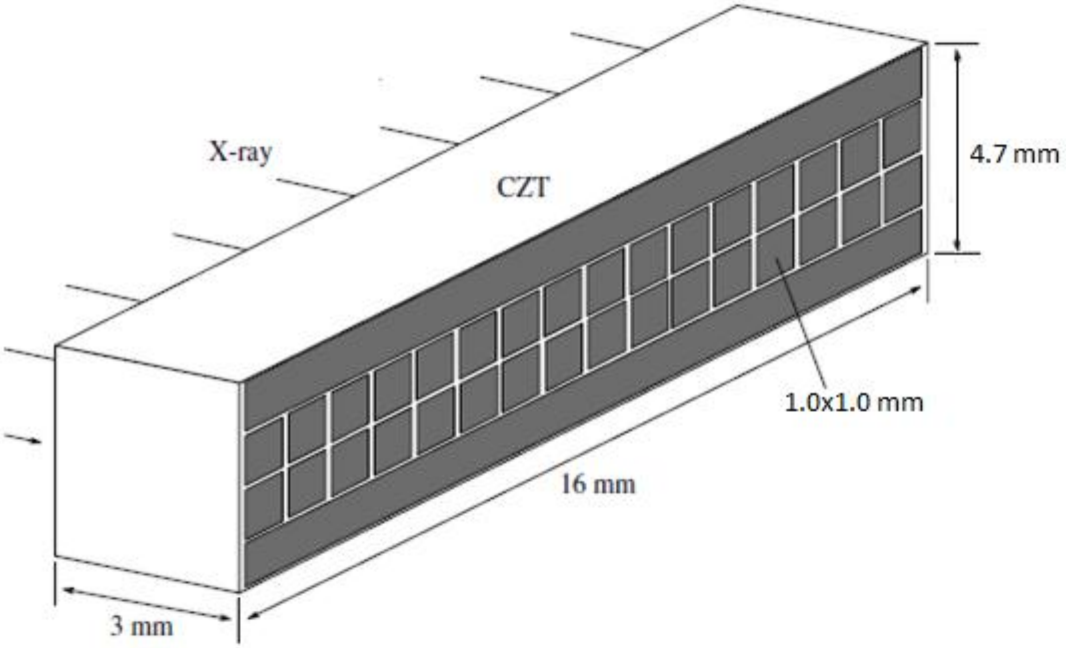

Figure 4. CZT crystal detector module. The PCSCT detector used by Dr. Shikhaliev featured 16 modules chained together to form a 2x256 pixel array with a field of view of 25.6 cm at the detector plane.

Using the photon counting CZT detector, 5 separate CT images can be created at 5 energy bins with one scan (Figure 5). This allows the added benefit of energy weighting or energy subtraction to be performed using data from one scan [42].

1.4. Adaptive filtration

Adaptive filtration is a method for equalizing the x-ray fluence to facilitate photon counting spectral CT [42, 45]. The CZT detector’s main limitation is its limited dynamic range in comparison to conventional CT detectors. Currently, CZT detectors can accept at most 2 Mcount/pixel/s for 1 mm^2 detector pixel size. However, count rates can be as high as 30 Mcount/pixel/s along the edges of the detector where x-rays pass through the thinner peripheries of the breast to arrive at the detector. Adaptive filtration makes the x-ray flux uniform over the detector surface [42, 43].

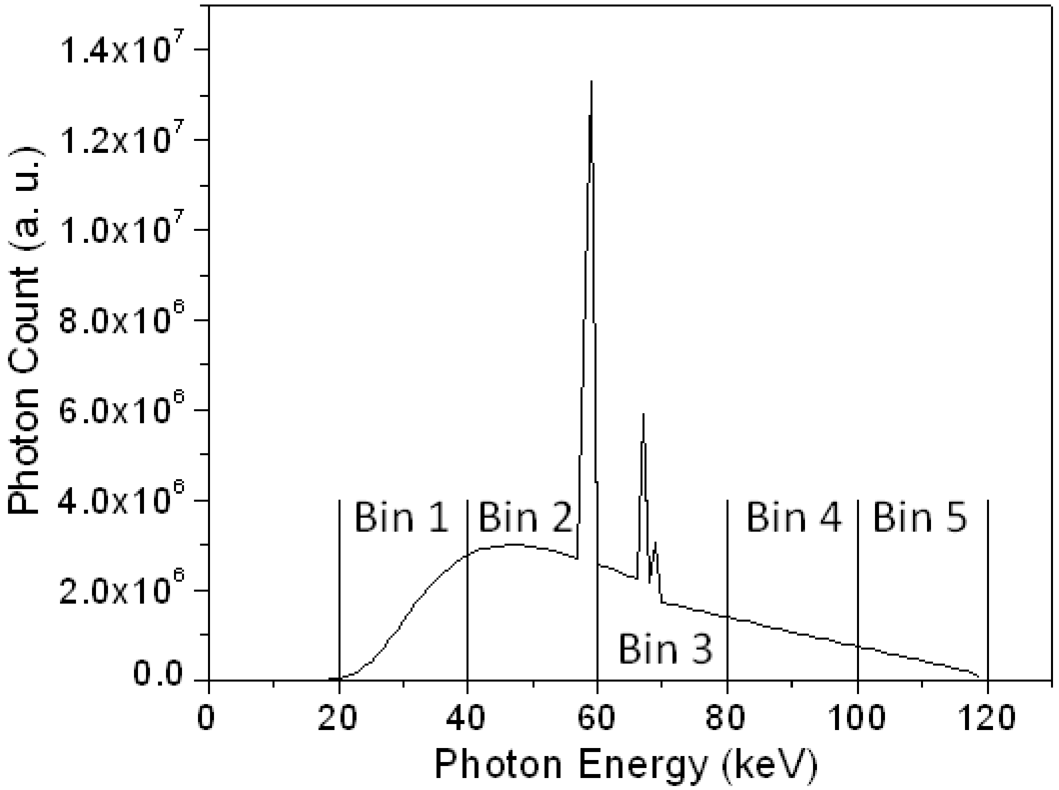

Figure 5. A simulated 120 kVp tungsten-anode spectrum created using SpekCalc [52], showing the spectrum split into five energy bins. Five independent CT images may be acquired using one scan, allowing energy weighting and energy subtraction to be performed on the CT image set.

Ensuring a uniform x-ray flux across the detector prevents the detector pixels that intercept flux from low attenuating areas, like the edges of a breast, from becoming overloaded by excessive photon count rates. Utilizing an adaptive filter made from material with radiological properties similar to tissue provides an additional benefit: beam hardening will be uniform across the detector as well. Uniform hardening eliminates cupping artifacts, which occur due to non-uniform hardening of the x-ray beam over the breast cross-section and present as a bowl-shaped distribution of CT numbers. Lastly, more uniform dose distributions over the breast tissue are expected when using adaptive filtration compared to the dose distributions observed without the adaptive filter present [45, 46]. Adaptive filtration is not appropriate for complex shapes or objects with large variations of attenuation coefficients, such as the chest or abdomen. However, adaptive filters are feasible for breast CT because breast tissue has relatively uniform composition and attenuation, and also has a relatively uniform round cross-section when imaged in pendant geometry [4, 7, 8, 10, 16, 17, 42, 47, 48]. Shikhaliev's proposed breast CT design includes a breast holder (Figure 6), unlike systems developed by others [7, 49], which further enforces a uniform cylindrical shape of the breast.

The adaptive filter closely resembles the "water bath" used in early CT systems [16, 50], and the "bow tie" filter currently used in commercial CT systems [51]. The adaptive filter differs from the bow tie filter in that it modifies the spectral content across the field of view to compensate for beam hardening while providing a nearly uniform intensity distribution like a bow tie filter. The bow tie filter does not compensate for beam hardening.

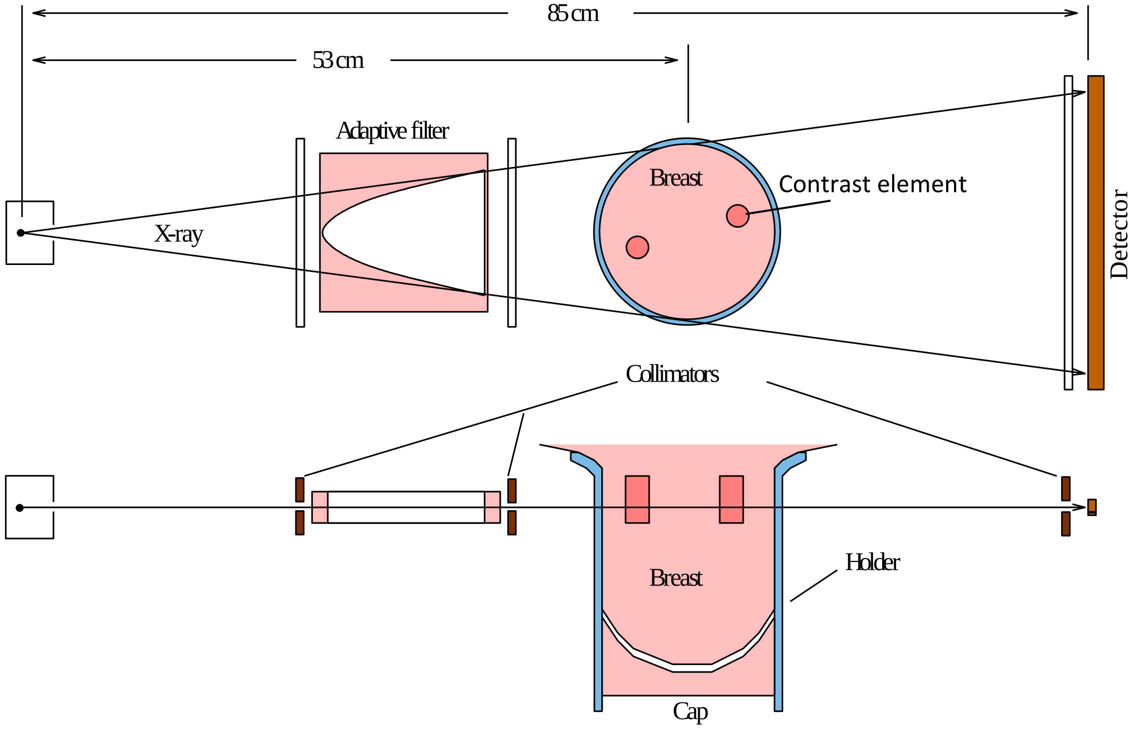

Figure 6. Schematics of the breast CT system with an adaptive filter [26].

1.5. Purpose of the research

The purpose of this study was to investigate adaptive filters for breast CT and to quantify their effect on CNR uniformity, CT number uniformity, and CT noise over the reconstructed CT images of the breast, as well as CT dose distribution over the breast volume. To achieve this goal, adaptive filters based on different materials were simulated and evaluated; also a filter made from tissue-like material was fabricated and tested. Spectral breast CT images with and without adaptive filtration, and with and without energy weighting were simulated at different tube voltages and entrance skin exposures. Material decompositions were performed for two types of contrast elements, with and without adaptive filtration, and at different tube voltages. The radiation dose distribution in the breast volume, as well as total breast dose, with and without adaptive filtration and at different tube voltages, was measured and compared.

1.6. Hypotheses and specific aims

Two hypotheses guided this work. First, we hypothesized that utilizing the adaptive filter while keeping average breast dose the same as without adaptive filtration provides similar or improved contrast to noise ratio by reducing image noise across the detector field of view. Improvement will be quantified by determining both the mean and standard error of each measurement recorded. Second, we hypothesized that utilizing the adaptive filter at the same average breast dose as without the filter provides a dose distribution across the breast that is no less uniform than the dose distribution seen without the adaptive filter. To test these hypotheses, five aims were completed.

Aim 1. Adaptive filter simulation. Design, simulate and evaluate adaptive filters that will provide uniform fluence across the detector surface. The filter materials investigated are acrylic, teflon, aluminum, and water.

Aim 2. Quantifying the effects of the adaptive filter on CNR, CT noise, and CT number. Simulate CT images of a breast with and without adaptive filtration, at different tube voltages, and at the dose levels accepted for screening mammography. Determine the effect that adaptive filtration has on CNR, CT noise and CT number for these simulations.

Aim 3. Determining effects of adaptive filtration on spectral CT performance. For an energy resolving photon counting spectral CT detector, simulate breast CT with energy weighting and material decomposition. Determine the CNR improvement for optimally weighted images relative to non-weighted images for each contrast element type used, with and without adaptive filtration.

Aim 4. Experimental testing of adaptive filter. Test an adaptive filter fabricated from acrylic, using an acrylic breast phantom and energy-resolving spectral data acquisition.

Aim 5. Dose measurements. Measure spatial dose distributions and average dose in a breast phantom with and without adaptive filtration at different tube voltages.

CHAPTER 2. METHODS AND MATERIALS

2.1. X-ray source

Simulations of breast CT with adaptive filtration required x-ray spectra that accurately represented achievable beam characteristics. For this purpose, SpekCalc, a software program verified to provide accurate x-ray spectra, was used [52]. Spectra were simulated with 6.27 mm aluminum equivalent filtration and an anode bevel angle equal to 10°.

Spectra were simulated over a range of tube potentials for several reasons. First, dedicated breast CT is an emerging technology and currently there is no consensus on what tube voltage should be used. Some researchers used 80 kVp [7] for an average diameter breast, while others used 49 kVp [49]. Second, photon counting spectral breast CT can provide higher CNR at the same dose level due to energy weighting compared to conventional CT [11, 30], so higher tube voltage can be used to decrease dose without sacrificing CNR. A higher tube voltage also facilitates better material decomposition [43]. For the current study, spectra were simulated at 40 kVp, 60 kVp, 90 kVp, and 120 kVp, resulting in filtered spectra with aluminum equivalent half value layers (HVL) of 2.16 mm, 3.42 mm, 5.08 mm, and 6.60 mm, respectively.

Figure 7 displays the x-ray spectra calculated by SpekCalc for this study. The spectra were calculated at 1 keV steps from 20 keV to the peak energy of the beam. The output spectrum included bremsstrahlung and characteristic x-rays with output air kerma specified in µGy/mAs at a distance of one meter from the source. The spectral output was converted to units of mR/mAs at a distance of one meter from the source by dividing the spectral output value by 8.76, then scaling to produce a total entrance skin exposure (ESE) to the breast of 660 mR [10] at the isocenter, 53 cm from the tube focal spot.

The CT simulations required knowledge of the number of x-ray photons arriving at each detector pixel. The SpekCalc software provided x-ray tube output in the units of x-ray photons per area (mm^2) per electron charge (mAs) at one meter from the tube focal spot. Thus, the number of x-ray photons per square millimeter per mR was known for each tube voltage. This allowed for determining the number of x-ray photons per detector pixel per CT projection. The 660 mR total ESE was assumed to be delivered equally over 180 CT projections with a detector pixel area of 0.5x0.5 mm^2 measured at isocenter.

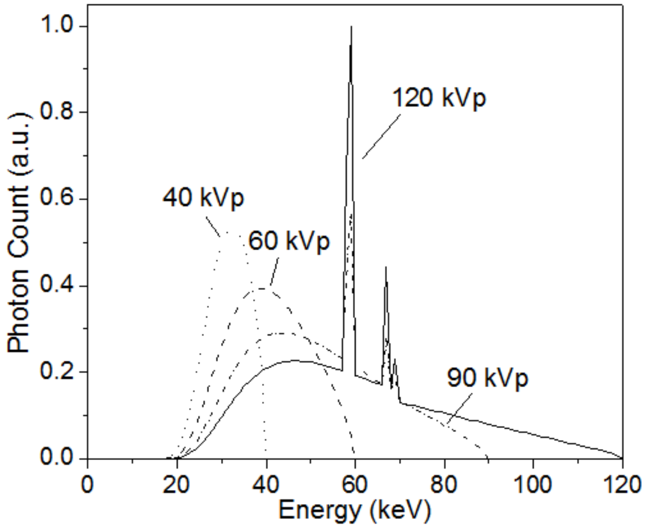

Figure 7. X-ray spectra at 40, 60, 90, and 120 kVp used for breast CT simulations. For display, the spectra were normalized to the total number of x-rays.

2.2. Adaptive filter

2.2.1. Theory and design of the adaptive filter

The geometry used for calculations of the adaptive filter shape is shown in Figure 8. In the simplest case one would assume that the filter was made from the same material as the breast phantom. In this case the filter thickness at any angle α was determined simply as the difference between the phantom diameter and the phantom chord length $\overline{QT}$, which is independent of x-ray energy. However, in real imaging applications the filter material will be different than breast tissue. In this case the angular dependence of the filter thickness should be calculated for a particular x-ray spectrum and take into account the energy dependence of the attenuation coefficients of the filter and phantom materials.

The chord length through the phantom for x-rays propagating along angle α was determined through a double application of the law of cosines:

$$\overline{QT} = 2\sqrt{r^2 - L^2 * sin^2(\alpha)} \tag{1}$$

where r is the phantom radius and L is the source to isocenter distance. The maximum angle allowed (which is the half fan angle of the beam) was found by solving Eq. 1 with the chord length set equal to zero:

$$\alpha_{max} = arcsin\left(\frac{r}{L}\right) \tag{2}$$

For a system with a 55 cm distance to isocenter and a 14 cm diameter phantom, the half fan angle equaled 7.31°.

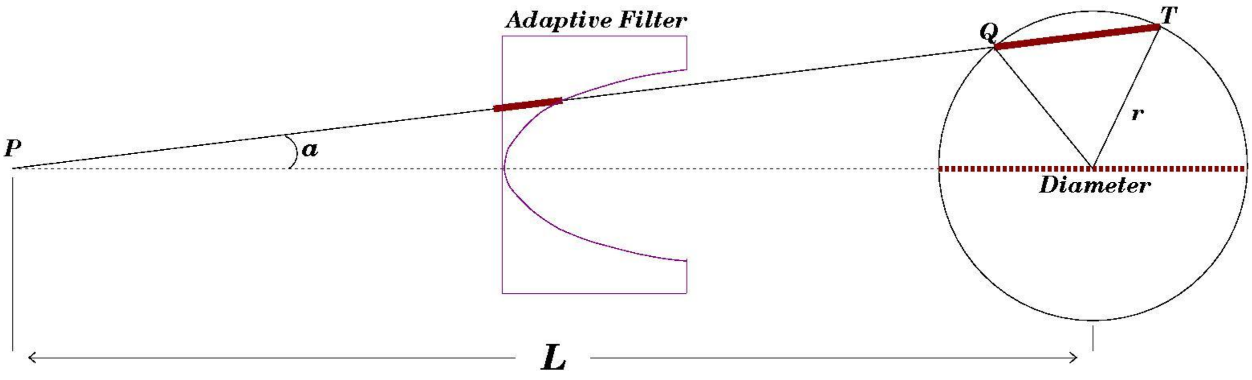

Figure 8. Illustration showing the geometry for calculating the thickness of the adaptive filter.

For the simplest case of the filter fabricated from the same material as the phantom, the filter thickness was

$$T \ = 2r - \ 2\sqrt{r^2 - L^2 * sin^2(\alpha)} \tag{3}$$

To calculate the angular dependence of the filter thickness for a filter material which was different than the phantom material, the x-ray energy spectrum was divided into multiple energy bins E_i with fixed bin width of 1 keV. The maximum half-fan angle α_{max} was divided into 13 sub-angles: 11 sub-angles from 0º to α_{max} with increments equal to 1/10 α_{max} and 2 sub-angles at angles of $0.95\alpha_{max}$ and $0.975\alpha_{max}$ to provide higher accuracy of the calculated filter thickness toward the periphery of the phantom. The number of x-ray photons N_i^α at energy E_i that passed through the filter and phantom at angle α was determined as:

$$N_i^\alpha \ = N_{0i}^\alpha \ e^{-(\mu_i t_\alpha + \mu_i' q_\alpha)} \tag{4}$$

where N_{0i}^α was the number of x-ray photons with energy E_i arriving from the x-ray tube at the filter at angle α , μ_i and μ_i' were the linear attenuation coefficients of the phantom and filter materials at energy E_i, respectively, and t_α and q_α were phantom and filter thicknesses at angle α, respectively. The total number of x-ray photons arriving at the detector surface at any angle α was required to equal the total number of photons arriving at α=0,

$$\sum_i N_i^\alpha \ = \sum_i N_i^{\alpha=0} \tag{5}$$

i.e., the x-ray intensity was flat across the detector surface. To meet this condition, the filter thickness q_α at the fixed angle α was adjusted iteratively until Eq. 5 was satisfied. Three filters were designed by this method, made from acrylic, teflon, and aluminum, respectively.

To fabricate an actual filter, the filter thickness *y* as a function of off-axis position *x* was required. This was calculated by:

$$y = q * cos(\alpha) \tag{6}$$

$$x = (SFD + y) * tan(\alpha)$$

where q is the length of the filter along the path at angle α (Figure 9). Off-axis distance x was determined by multiplying the sum of the source to filter distance (SFD) and perpendicular filter thickness y with *tan*(α). Once y and x were calculated, a second order polynomial interpolation between individual calculated points formed a smooth boundary for the distal side of the filter.

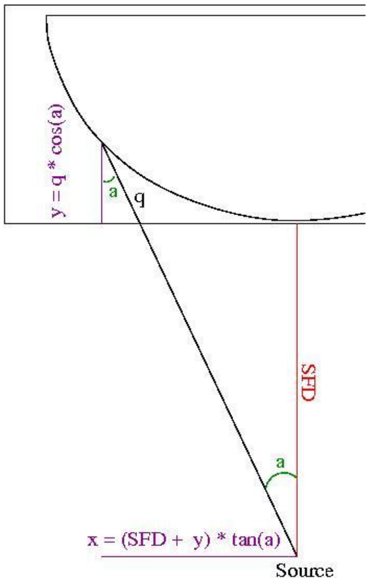

Figure 9. Geometry for conversion of filter thickness vs. angle to perpendicular filter thickness *y* vs. off-axis distance *x*.

2.2.2. X-ray beam characterization with adaptive filtration

a) Beam hardening with adaptive filter

Beam hardening occurred as x-rays passed through the adaptive filter and breast. The amount of beam hardening was independent of fan angle if the filter and phantom materials were the same. However, if the filter and phantom materials were different, the magnitude of the beam hardening depended on the angle at which the x-rays passed through the materials. If the material was less attenuating than breast tissue, then the magnitude of the beam hardening decreased as the angle increased, and vice versa. Beam hardening was determined for the 120 kVp beam at the detector plane with filters made from acrylic, teflon, and aluminum. The same sub-angle scheme as used for the determination of the filter profiles in the previous section were used to determine the half-value layer of the resulting spectral distribution across the surface of the detector. Each sub-angle's photon flux after exiting the adaptive filter and phantom was attenuated through an aluminum filter whose thickness was iteratively varied to find the thickness that reduced the beam intensity by half. The resulting aluminum equivalent half-value layer distribution vs. half-fan angle for each filter type was plotted for comparative purposes. Along with beam hardening versus half-fan angle, the resulting spectral distributions of a 120 kVp beam at half-fan angles of 0, 5.81 and 7.31 degrees were plotted together to demonstrate the beam hardening that occurs for the various filter materials with increasing angle from the fan-beam central axis.

b) Beam intensity variations with adaptive filter

When the adaptive filter and phantom materials are different, the resulting flat x-ray intensity at the detector surface and the modified x-ray spectrum to minimize beam hardening non-uniformity can be provided only at the tube voltage for which filter was designed. At other tube voltages, the intensity and spectral distributions deviate from the desired distributions. The amount of deviation depends on the type of filter material and the tube voltage. To study this effect, filters were designed to provide flat intensity distributions at 120 kVp for acrylic, teflon, and aluminum materials. Then the intensity distributions resulting from using the 120 kVp filters at 40 kVp, 60 kVp, and 90 kVp were calculated. These intensity distributions were plotted against half-fan angle, and deviations from flatness were quantified.

c) Exposure scaling factors

The ESE measured at isocenter along the central axis is the same with or without the adaptive filter. However, attenuation in the adaptive filter decreases ESE toward the periphery of the field of view. For this reason, the mean ESE across the breast surface with the adaptive filter will be less than when no filter is used. Therefore, one could reasonably increase the tube output when using the adaptive filter such that the mean ESE returns to the same level as without the adaptive filter. Increased tube current corresponds to improved image quality. To return the mean ESE with the adaptive filter to 660 mR, scaling factors for increased tube output were determined by modeling filtered and unfiltered spectra in SpekCalc. The scaling factors for this increased tube output were determined such that the resulting mean exposure along the surface of the phantom was 660 mR with the adaptive filter in place. Attenuation thickness was determined through the breast phantom along chord lengths that passed through a ray originating at the center of the phantom and travelled perpendicular to α_{max} at 0.5 cm intervals from 0 to 7 cm, inclusive, as shown in Figure 10.

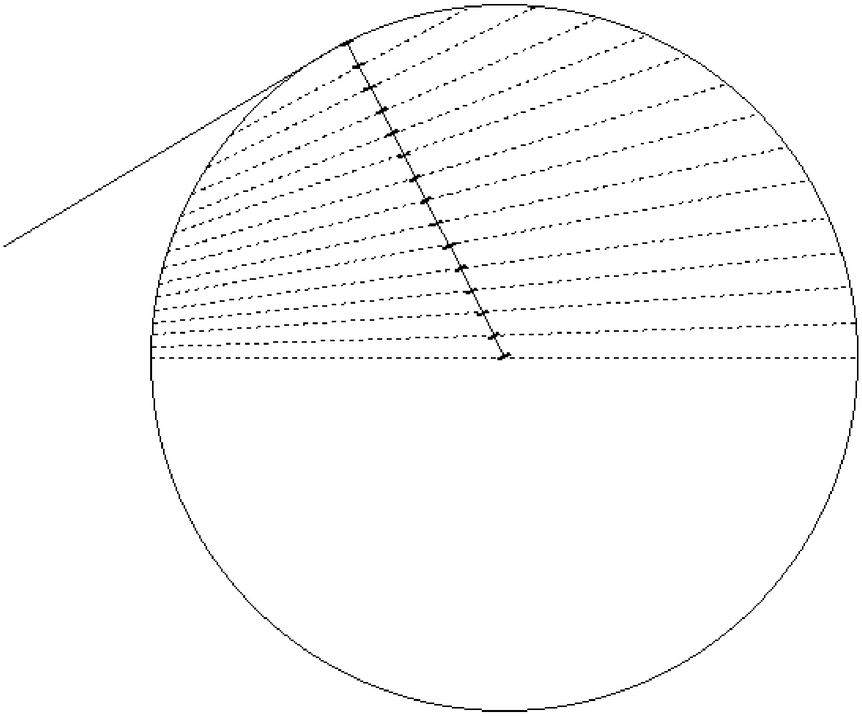

Figure 10. Ray originating from the center of the 14 cm breast phantom, travelling radially outward and passing perpendicular to α_{max}. The ray was subdivided into 0.5 cm intervals and attenuation lengths in the phantom were determined for rays that originated at the tube source and passed through each 0.5 cm endpoint. (Image not to scale)

Filter thickness q was calculated according to Eq. 7

$$q = 2r - \text{chord length}_x. \tag{7}$$

The filter thicknesses recorded at those intervals were entered, one at a time, into the SpekCalc software, as water filtration while holding aluminum equivalent inherent filtration, minimum energy, peak energy and bevel angle the same as before for each of the four tube voltages. Water was used as the attenuating material because the filter was simulated from liquid water. The spectrum simulation was run for each recorded angle, and the resulting bremsstrahlung and characteristic dose data were recorded, and the mean value of all the recorded measurements was calculated. An exposure increase scaling factor was determined by dividing the sum of the bremsstrahlung and characteristic dose without the filter present by the average bremsstrahlung and characteristic dose across the field of view with the adaptive filter in the beam. The exposure increase scaling factors plotted against tube voltages are shown in Figure 11.

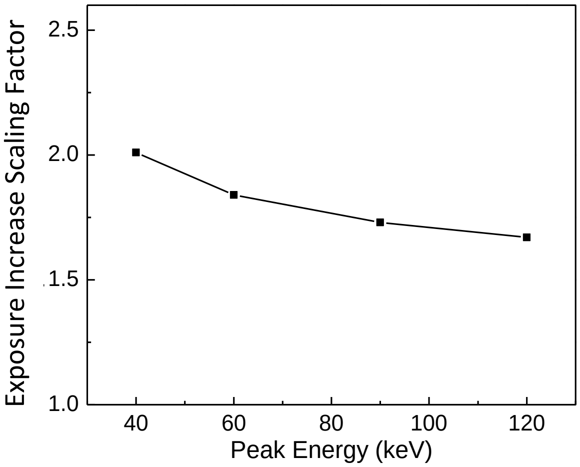

Figure 11. Exposure scaling factor versus tube voltage.

2.2.3. Fabrication and experimental testing of adaptive filter

An acrylic adaptive filter was designed and fabricated to be used with a 14 cm diameter cylindrical homogenous acrylic phantom. The side of the adaptive filter proximal to the tube source was placed 23 cm from the x-ray tube focal spot. A long focal spot-to-filter distance was found in practice to lessen the impact of lateral and radial errors in filter placement on photon fluence uniformity at the detector. This location also was far enough from isocenter to reduce the chance of scatter reaching the phantom and detector, lessening scatter dose to the phantom and excess count rate at the detector. The uniformity of x-ray flux at the detector after traversing the filter and phantom combination was compared to the x-ray flux transmitted through a uniform acrylic slab with 14 cm thickness. Uniformity was assessed for simple (non-binned) photon counting of all photons from 26 keV to 120 keV in energy, as well as for spectral imaging with the detected photons binned according to Table 2 for 120 kVp (see section 2.4.1). Before obtaining the measurements, the detector signal was flat-field corrected. (For a brief description of flat-field correction, see Appendix A.) A qualitative assessment of the results was used to identify positioning errors of the filter. These results were also used to assess noise uniformity across the detector when using the adaptive filter.

2.3. Effects of adaptive filtration on CT number, noise, and CNR

CT simulations were used to study the effects of adaptive filtration on CT number, CT noise, and CNR. An adaptive filter made from water was designed to match a simulated 14 cm diameter cylinder of water. Water was selected as the background material of the phantom, rather than breast tissue, so that future experimental work using a water equivalent phantom could be compared to these simulated studies. Because the adaptive filter and phantom were made from the same material, beam hardening had no effect and the filter thickness for a given angle was calculated form the chord lengths of the phantom (Eq. 3).

The phantom included two types of cylindrical contrast elements (Figure 12). One contrast element was adipose tissue, whose composition was obtained from ICRU Report 44 [53]. The other contrast element was an iodine-water solution with an iodine concentration of 2.5 mg/cm^3. This concentration was selected because it approximates the average uptake of iodinated contrast media by breast carcinoma [11]. Each cylindrical contrast element was 15 mm in diameter. The contrast elements were placed at five radial distances from the phantom's center: 1 cm, 2.25 cm, 3.5 cm, 4.75 cm and 6 cm. Their positions were offset in a spiral pattern so that no more than two contrast elements of the same type overlapped in any projection view.

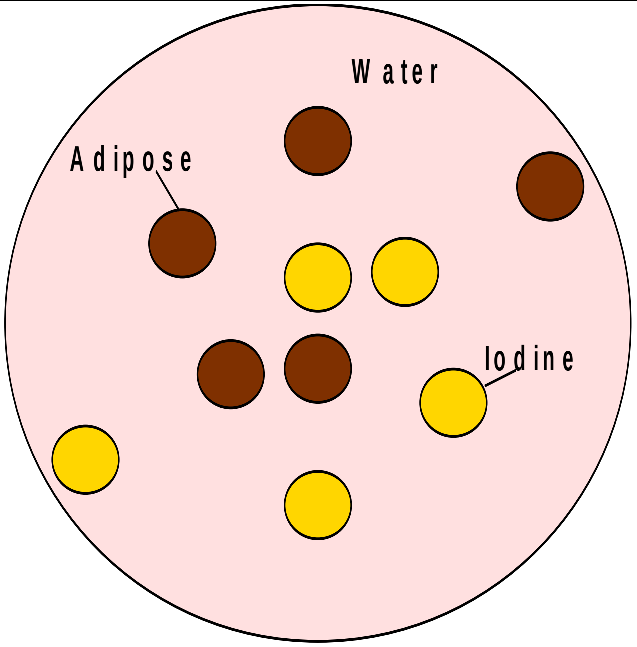

Figure 12. Simulated breast phantom comprising a 14 cm diameter water cylinder with adipose and iodine contrast elements placed at 5 distances from the center of the phantom.

The CT simulations were performed for three situations: 1) no adaptive filter in the beam with a tube output giving 660 mR mean ESE, 2) the adaptive filter in the beam with the same tube output, and 3) the adaptive filter in the beam with tube output increased by a scaling factor to give a 660 mR mean ESE.

2.3.1. CT simulations

For simulations of the CT images the linear attenuation coefficients for adipose, water and iodine were obtained from NIST's XCOM database from 1 keV to 120 keV [54]. Narrow beam geometry was assumed because fore and aft collimation (Figure 6**)** greatly limit scatter reaching the detector. The scatter to primary ratio using the geometry in Figure 6 would be well below 7%, and any residual difference between simulation results using narrow beam data and experimental results could be accounted for by a scaling factor [11]. The phantom was simulated for 40 kVp, 60 kVp, 90 kVp, and 120 kVp beams binned into 3 keV steps, starting at 20 keV. With the exception of 40 kVp, the highest energy bin had a bin width of 2 keV. A copy of the phantom was created for each energy bin, where input pixel values were the average attenuation coefficient for that bin for the material comprising that pixel. The pixel size used for simulation equaled 0.5x0.5 mm^2. An array of 512x512 pixels was used for all CT imaging simulations. Pixels were comprised of either air outside the phantom, water background, adipose contrast element or a 2.5 mg/cm^3 iodine solution in water, with no mixing of the materials inside pixels. The phantom for each bin was forward projected by Radon transformation using MATLAB's parallel beam geometry Radon transform function with 180 projections [55]. Utilizing parallel beam geometry Radon function for transformation and reconstruction of the image sinograms produces results identical to those for the fan-beam Radon function. The resulting sinograms were exported to ImageJ because subsequent manipulations of the data were more easily performed inside this program [56]. The data were exported from MATLAB in a 16 bit unsigned TIFF format, as this was the easiest way to read in and out files from ImageJ, and MATLAB could only export 16 bit unsigned integer TIFF files. The sinograms were normalized to a value of (μ_{water}^{i}*diameter) for pixels at the center of the phantom that corresponded to rays that did not pass through any contrast elements, where μ_{water}^{i} was the attenuation coefficient of water for the i^{th} energy bin. Sinograms represent the total linear attenuation coefficient along lines through the phantom. Therefore, the sinograms were converted to transmission factors; multiplying by the initial intensity of the primary x-ray beam then gave the number of photons reaching the detector.

To generate a perfectly matched adaptive filter, the inverse of the sinogram of a uniform water phantom was used as the adaptive filter's sinogram. For simplicity, parallel beam geometry was assumed here; the method in section 2.2.1 used to construct the adaptive filter's sinogram was the parallel beam geometry equivalent of the adaptive filter. To generate the adaptive filter's sinogram, the phantom without contrast elements was first generated in ImageJ with pixel values equal to the mean linear attenuation coefficients for 3 keV energy bins, for each tube voltage. The resulting object data were imported into MATLAB and Radon transformed to generate sinograms. The sinograms were then exported back to ImageJ and normalized so that the pixel values of the sinogram corresponding to the rays that pass through the diameter of the phantom equal μ_{water}*diameter. The conversion from phantom sinograms to adaptive filter sinograms was made by subtracting each given pixel value from the maximum pixel value of the original sinogram. Finally, the adaptive filter's sinogram was converted to an adaptive filter transmission factor TF according to Eq. 8

$$\text{TF} = e^{-\text{sinogram}}. \tag{8}$$

To apply the adaptive filter to the phantom data, the photon count rates produced by the phantom transmission factor were multiplied by the transmission factor of the adaptive filter for each energy bin. For scaled exposures, the simulated detector count rates were multiplied by the exposure scaling factor determined for the tube voltage (see Figure 11 in section 2.2.2.)

Statistical noise was added to the sinograms before CT reconstruction. For each pixel in a sinogram, a random number was generated for a Gaussian distribution with standard deviation of 1 and a mean of 0. This random number was multiplied by the square root of the photon counts for the corresponding pixel and then added to the photon counts. Noise was independently calculated for the sinograms of every simulation set and for each 3 keV bin.

After all the 3 keV bin sinograms were converted to photon counts with statistical noise, they were summed together to produce a polyenergetic sinogram. If the adaptive filter was used, the summed photon count sinogram was divided by the filter transmission factor of the energy bin representing the average energy of the beam used. This was equivalent to normalizing a commercial CT scanner with an air scan to remove the influence of the aluminum bowtie filter used in commercial CT systems from the final reconstructed image.

Prior to reconstruction, the noisy count rate data were converted into corresponding noisy sinograms (μ-maps) by Eq. 9

$$\text{sinogram} = -\ln(\mathrm{N}) + \ln(\mathrm{N_o}) \tag{9}$$

where N equaled the photon count after passing through the filter and phantom material and N_o was the background photon count that passes through only air. The noisy sinograms were exported into MATLAB and reconstructed using the iradon function with the Shepp-Logan reconstruction filter [55].

To calculate CNR, noiseless reconstructed images were simulated as well. The above steps were followed, but the steps to add statistical noise were omitted. Noise-only images were made by subtracting the noiseless reconstructed images from the corresponding noisy reconstructed images in ImageJ.

2.3.2. Evaluation of the CT images

To perform quantitative evaluation of CT images, the final reconstructed images were exported to ImageJ for conversion to Hounsfield units (HU). To convert to HU, the mean attenuation coefficient was obtained for a circular region of interest (ROI) with a radius of 3.5 cm over the water background of the phantom. Care was taken to not include any contrast elements in the background region. The mean background value was set equal to μ_{water} associated with the average x-ray energy used to reconstruct the image. The HU were calculated by [9]

$$\text{HU} = \frac{(\text{pixel value} - \mu_{\text{water}})}{\mu_{\text{water}}} * 1000. \qquad (10)$$

Once the pixel values in the reconstructed images were converted to HU, the images were assessed for CT number uniformity, CT noise, and CNR. CT number profiles were obtained across the horizontal diameter of the phantom where the profile only passes through water. The average CT numbers for water in the noisy reconstructed images were determined at the radial distances corresponding to each of the 5 contrast element positions. With the exception of the position closest to the center, the mean background value was measured with a semicircular arc ROI with a radius of curvature equal to the radial distance of each contrast element position (Figure 13). Due to the smaller pixel numbers around the contrast element closest to the center, two circular regions of interest with a diameter of 15 mm were obtained at the same radial distance as the position of the contrast element. Two regions of interest were used to try to increase the statistically relevant data. The mean value was obtained over the two regions of interest and recorded as the CT number of the background water at this smallest radial distance. Results were obtained for each tube operating potential and each of the 3 simulated sets.

Contrast to noise ratio (CNR) was calculated in four steps for each contrast element position, type, simulated set, and tube operating potential. First, using the noiseless reconstructed images, the mean HU value was determined for a 25 pixel (12.5 mm) diameter ROI centered over each contrast element (Figure 13). Next, the background value was measured using the background ROI shown in Figure 13. Contrast was calculated as mean signal S_c within the contrast element subtracted by mean background signal S_b. The CNR was then determined as

$$\mathrm{CNR} = \frac{S_c - S_b}{\sigma} \tag{11}$$

where σ is the measured noise at the same radial distance as the contrast element.

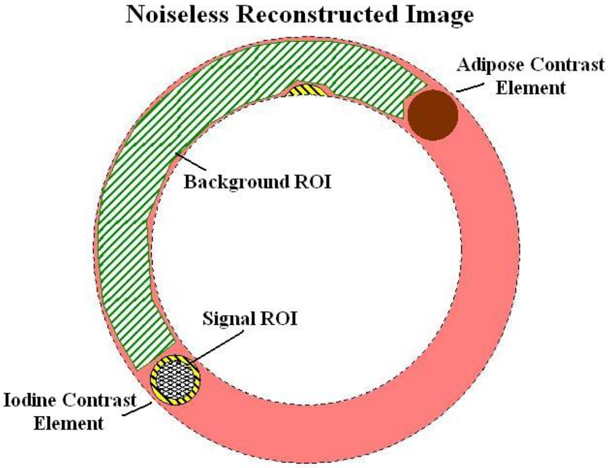

Figure 13. Contrast equals the average CT number measured with a circular ROI over a contrast element minus the mean background water CT number measured over a semicircular arc ROI at the same radial distance.

Noise was determined by making a ring ROI (Figure 14) in the noise-only reconstructed image with an annular width of 30 pixels (15 mm) and a radius of curvature equal to the radial distance to the contrast element for which CNR was measured. Noise, being proportional to the square root of the image magnitude, was measured at the same radial distance as the corresponding contrast element to avoid uniformity variations across the phantom, especially for the simulation set without the adaptive filter.

Uncertainty (standard error) for the mean values of both signal and background were determined by dividing the standard deviation of the pixel values recorded for the appropriate ROI by the square root of the area (i.e., total number of pixels) of the ROI. The uncertainty of the contrast $(S_c - S_b)$ was then determined by error propagation from the uncertainties of signals S_c and S_b over the contrast elements and background area, respectively.

Uncertainty in the noise σ in Eq. (11) was determined from measurements of σ in 8 ROIs along the ring ROI defined above, as shown in Figure 14. The standard error of σ was calculated from these 8 measurements. Uncertainty in CNR was determined from the uncertainties of S_b , S_c, and σ by applying error propagation rules to Eq. (11).

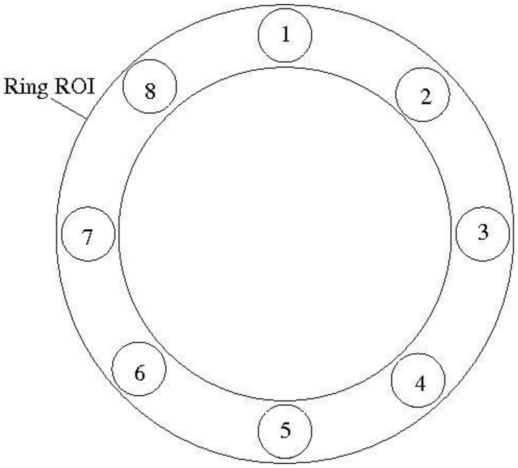

Figure 14. Ring ROI for the noise-only reconstructed image for a particular radial position. Uncertainty in the noise measurement was the standard deviation determined from ROIs at the 8 cardinal directions.

Extrapolations of the curve were taken with a second order polynomial fit to the data to approximate the value of the noise for each of the 3 sets of simulations at the center of the phantom as well as at the edge of the phantom (7 cm radial distance).

2.4. Spectral CT with adaptive filtration

2.4.1. Energy bin arrangements

To achieve energy selective CT acquisition, the CT detector splits the energy spectrum into multiple energy bins. Five to six energy bins are likely sufficient for clinical applications of spectral radiography and CT [57]; prototype spectral CT systems with 5 bins [36, 42] and 6 bins [58] have been reported. In our simulations we used the system parameters described in [42]. To generate spectral CT image data, the same steps were initially followed as for the simple photon counting image creation listed in section 2.3.1. When the sinograms were converted to photon counts, however, they were summed according to the binning scheme in **Table 1**.

Table 1. Binning scheme used for energy weighting and material decomposition.

Binning Scheme				
	40 kVp	**60 kVp**	**90 kVp**	**120 kVp**
Bin 1	20 - 26 keV	20 - 33 keV	20 - 33 keV	20 - 40 keV
Bin 2	27 - 32 keV	34 - 42 keV	34 - 43 keV	41 - 60 keV
Bin 3	33 - 40 keV	43 - 51 keV	44 - 55 keV	61 - 80 keV
Bin 4	-	52 - 60 keV	56 - 70 keV	81 - 100 keV
Bin 5	-	-	71 - 90 keV	101 - 120 keV

2.4.2. Material decomposition

Spectral CT allows for material decomposition using only one scan, a benefit that reduces dose to the patient compared to traditional material decomposition techniques. Material decomposition was performed for CT acquisitions with and without the adaptive filter. The spectral reconstructed images described in the previous section were grouped into low and high energy data according to the scheme outlined in **Table 2**.

Table 2. Grouping scheme used for material decomposition. The spectral bins were grouped into low and high energy data.

	40 kVp	60 kVp	90 kVp	120 kVp
Low E	20-32 keV	20-42 keV	20-55 keV	20-60 keV
High E	33-40 keV	43-60 keV	56-90 keV	61-120 keV

Low and high energy images to use for dual energy subtraction were generated for noiseless and noisy reconstructed images for all tube operating potentials. The weighting factor for dual energy subtraction equals $\frac{\text{Signal (High Energy Image)}}{\text{Signal (Low Energy Image)}}$ for one type of contrast element, measured using the noiseless reconstructed image sets. Gaussian smoothing was applied with a $2\sqrt{2}$ pixel radius to both the low and high energy reconstructed images to suppress noise in the decomposed images. The low energy image was scaled by the weighting factor, then the difference between the low and high energy images was taken to generate the material decomposed image. For each contrast element type, a separate weighting factor and material decomposed image were created for each of the three simulated sets: without and with the adaptive filter and with scaled tube output. For the material decomposed images, measurements of CNR and its associated uncertainty were performed using the same techniques described in section 2.3.2.

2.4.3. Energy weighting

Energy weighting was examined to maximize CNR in the reconstructed image and to test the effect of adaptive filtration on energy weighting. Each of the spectral reconstructed images for each tube voltage was utilized in energy weighting. A unique weighting factor was determined for each contrast element in the phantom based on its CNR in the spectral CT images. The optimal weighting factor w_i [30]to provide the highest CNR was

$$w_{i,x,p} = \frac{\mathrm{CNR}_{x,p}}{\sigma_{x,p}} \tag{12}$$

where i is bin number, x is contrast element type (adipose or iodine), and p is contrast element position (see Figure 11). Contrast was determined using the noiseless reconstructed images, and standard deviation was determined using the noise-only reconstructed images. CNR, standard deviation and uncertainty in CNR were all calculated using the same method described in section 2.3.2. Once found, the weighting factors were applied to the binned reconstructed images for each contrast element type and position. The weighted binned images were then summed together to create the final energy-weighted image. Energy weighting was applied to the data for each tube operating potential, each contrast element type and position, and for CT scans with and without adaptive filtration. CNR and associated uncertainty for the energy weighted reconstructed images were calculated.

2.5. Breast dose with adaptive filtration

The effect of the adaptive filter on breast dose was directly measured using the Computed Tomography Dose Index (CTDI) method [9] and a 6 cc RadCal ion chamber (Monrovia, CA); this pencil ionization chamber is designed for CT dose measurements. The measurements were performed using the experimental CT imaging setup from section 2.2.3. The CTDI method requires a scaling factor based on the x-ray beam profile, which was measured using a storage phosphor reader (Cyclone, Perkin Elmer, Shelton, CT). The storage phosphor detector plates were placed at the isocenter of the CT scanner and exposed to record the x-ray beam profile for each tube voltage. It was determined that the full width at half-maximum (FWHM) of the beam was 2.2 mm for all tube voltages, as shown in Figure 15, yielding a CTDI scaling factor of 45.5. CTDI was calculated by dividing the 100 mm length of sensitive field of view of the detector by the FWHM of the beam.

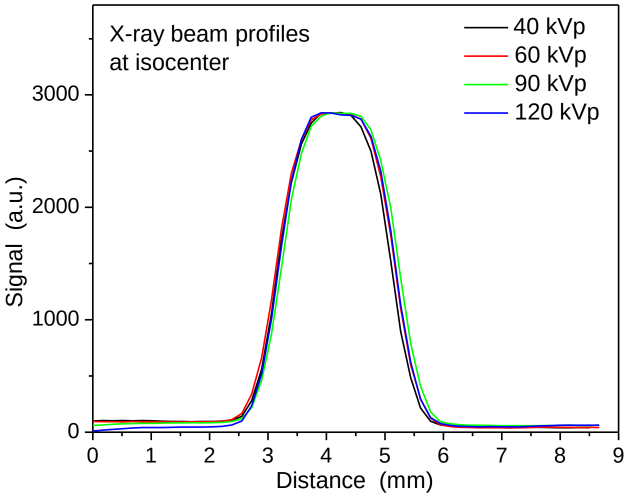

Figure 15. X-ray beam profiles for all 4 tube voltages used for breast dose measurements with the CTDI approach. The profiles were measured with a storage phosphor detector placed at the isocenter of the scanner. For every tube voltage, the FWHM of the beam was 2.2 mm.

Dose measurement was obtained using a 14 cm diameter cylindrical acrylic phantom with a length of 14.2 cm (Figure 16). The ion chamber fit completely into the phantom. Five cylindrical holes were drilled into the phantom at radial distances of 0 cm, 1.75 cm, 3.50 cm, 4.75 cm, and 6.00 cm. The holes were 9.5 mm in diameter, allowing a snug fit of the 9.25 mm diameter ion chamber. For each tube voltage, two sets of CT dose measurements were taken: one without the adaptive filter and one with the acrylic adaptive filter placed at 23 cm from the tube source. Multiple authors have assessed radiation dose applied to the breast in CT imaging applications [6, 59-61]. In dedicated breast CT, the total ESE is similar to that used in two-view mammography. In the absence of the adaptive filter this exposure is uniform along the breast surface. However, when the adaptive filter is used, the ESE will decrease toward the periphery of the breast. Thus, an adaptive filter decreases the mean dose to the breast, and also modifies the volume distribution of the dose.

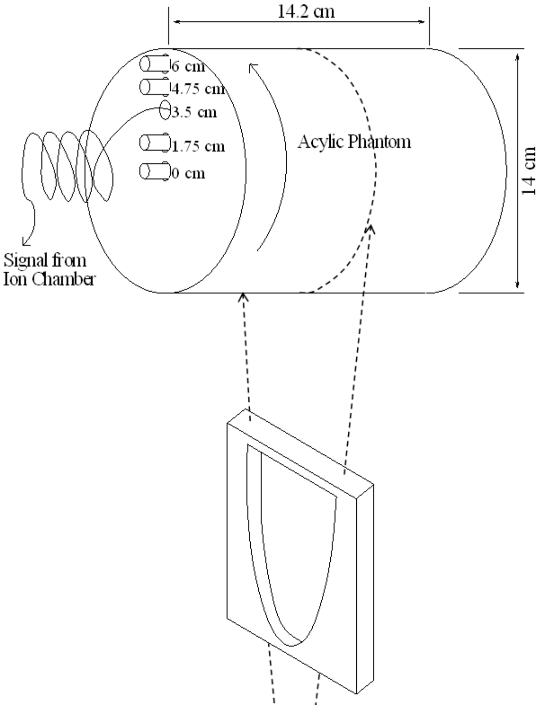

Figure 16. Illustration of the breast dose measurement phantom with adaptive filter.

For each tube operating potential, without and with the adaptive filter, and for the adaptive filter with the exposure scaling factor, ion chamber measurements were taken at each radial location in the phantom. The holes not occupied by the ion chamber were plugged with cylindrical acrylic rods. The ionization chamber measurements were converted to CTDI values by multiplying the recorded charge by the CTDI scaling factor. Plots of absorbed dose vs. radial distance were generated for each filter geometry and tube operating potential. A third order polynomial fit was applied to the five recorded dose measurements for each plot. Extrapolation of the fit curve generates a data point at 7 cm radial distance for each measurement. Using a custom MATLAB program, the polynomial fits were revolved about the center of the phantom to create 2D dose maps. The mean dose was calculated from the entire cross section of the phantom.

CHAPTER 3. RESULTS

3.1. Adaptive filter characterization

3.1.1. Filter shapes and placements

Figure 17 shows adaptive filter profiles for filters made from acrylic, Teflon, and aluminum at three distances from the tube focal spot. A distance of 5 cm was the closest one can reasonably get to the tube focal spot when taking into account the dimensions of the x-ray tube. An adaptive filter placed at this location would give the patient the lowest contribution of dose due to x-rays scattered by the adaptive filter. Also, this location would provide the lowest scatter contribution reaching the detector. However, in this case small errors in placement of the filter laterally and in depth with respect to the breast could result in relatively large inhomogeneities in photon flux reaching the detector.

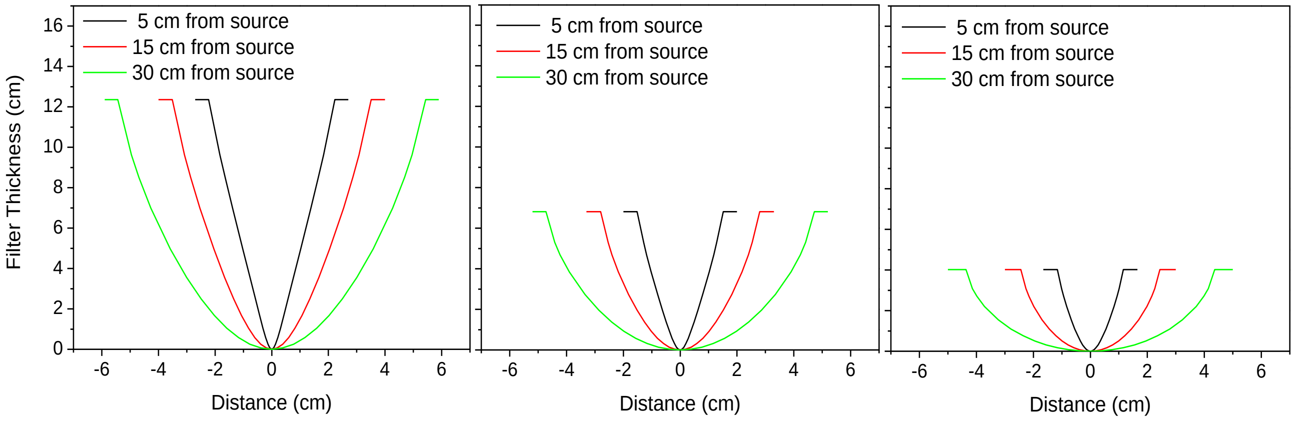

(a) (b) (c)

Figure 17. Filter shapes designed for the 14 cm diameter phantom and located at various locations on the beam axis. The shapes are superimposed to show shape and width changes of the filters with respect to distance from the source. At each distance, acrylic filters (a) were the largest, teflon filters (b) were the second largest and aluminum filters (c) were the smallest.

A distance of 30 cm from the tube anode represented the closest one could reasonably place the filter near the breast surface. Adaptive filters placed at this location would contribute the highest scatter dose to the breast; however, the uniformity in photon flux over the field of view of the detector would be least sensitive to incorrect placement of the adaptive filter, due to the shallower slope and larger size of the filter profile.

The third filter profile was simulated at 15 cm from the tube anode. This location represented a tradeoff between filter-scattered dose to the breast tissue and potential non-uniformity in photon flux at the detector due to small errors in filter placement laterally or in depth with respect to the breast phantom.

Filters made from acrylic were the largest in size, followed by teflon, then aluminum. Filter width and depth depended on both the material and the focal spot to filter distance. However, the attenuating properties of acrylic are more similar to breast tissue than either teflon or aluminum, and therefore acrylic produces a photon spectrum incident upon the detector surface that is more similar that which passes through breast tissue.

One issue to be addressed in future work, however, is that an adaptive filter designed for one breast diameter would be suboptimal for other breast diameters. To account for this, one would design adaptive filters to cover a range of breast diameters. The filters for an array of different breast sizes could easily be stacked in a holder for the helical-acquisition fan beam photon counting spectral breast CT shown in Figure 6 with either automatic or manual selection for each patient. Each of the filters would provide uniform x-ray intensity at the detector surface and optimized CT image quality.

3.1.2. X-ray intensity distributions with adaptive filter

Figure 18 shows the relative photon fluence reaching the detector after passing through the filters made from acrylic, teflon, and aluminum for the 4 tube voltages used in this work. The adaptive filters were designed to provide a uniform photon fluence across the detector surface for a 120 kVp tube voltage. Note that simulations were performed for a soft (glandular) tissue phantom, while normal breasts typically are composed of 50% adipose and 50% glandular tissue.

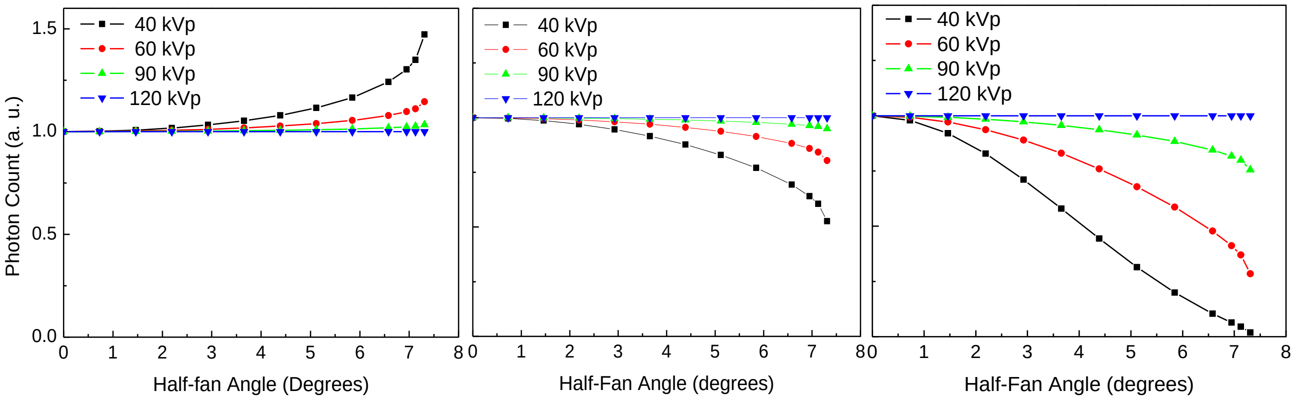

(a) (b) (c)

Figure 18. The total number of transmitted photons in the beam after the adaptive filter and phantom at four different tube voltages, and for three filter materials acrylic (a), teflon (b), and aluminum (c). Filters were designed for a 120 kVp beam, and a 100% glandular breast with 14 cm diameter, but used for all tube voltages.

Because a 50/50 adipose/glandular breast would have an effective Z closer to acrylic, and further from teflon or aluminum, the fluence distributions in Figure 18 depict the worst case for acrylic filters, and the best case for teflon and aluminum filters with respect to producing a flat fluence at non-optimal tube voltages. At tube voltages below 120 kVp, the flux did not remain uniform over the detector surface; non-uniformities increased as the tube voltage decreased from 120 kVp to 40 kVp. The relative magnitude of non-uniformity was approximately the same when comparing acrylic filtration and teflon filtration at the same tube voltage. For acrylic, the relative photon flux increased as the angle from central axis increased due to the fact that the effective atomic number Z for acrylic is lower than that of soft-tissue. The photoelectric interaction cross-section is proportional to Z^3. Therefore, as the angle increased, more acrylic and less soft-tissue was in the path of the photons, which lowered the overall probability that a photoelectric event would take place. This resulted in a relatively higher number of x-rays reaching the detector surface as the angle increased. Because the other two filter materials each had an effective Z higher than soft-tissue, the opposite effect was seen with increasing angle. The magnitude of the non-uniformities increased for all three filter materials as the tube voltage was lowered because the photoelectric cross-section is approximately inversely proportional to the cube of the photon energy in this energy interval.

3.1.3. Effect of adaptive filtration on beam hardening

The transmitted x-ray spectra for these adaptive filters are presented in Figure 19**.**

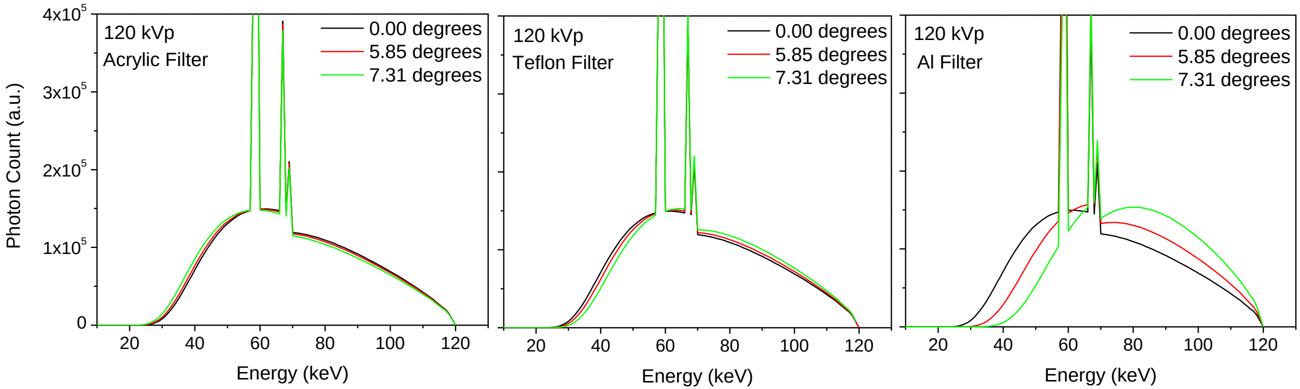

(a) (b) (c)

Figure 19. Transmitted spectra for three paths (angles) through each adaptive filter with the 14 cm diameter phantom. For acrylic (a), the beam softened as it passed through more filter and less tissue. The beam hardened slightly with teflon (b) and substantially for aluminum (c).

Spectra are shown at angles form the central axis of 0, 5.85, and 7.31 degrees, corresponding to increasing path lengths through the filter and decreasing path length through the phantom. The spectra for the acrylic adaptive filter changed the least over the detector field of view, followed by teflon and aluminum.

Figure 20 compares the beam hardening expressed in aluminum equivalent HVL for the photon spectrum after transmission through the filters made from acrylic, teflon, soft tissue, or aluminum, and a breast phantom for a 120 kVp tube voltage. At higher angles, more filter material was in the beam's path due to the decreasing thickness of breast tissue with increasing angle.

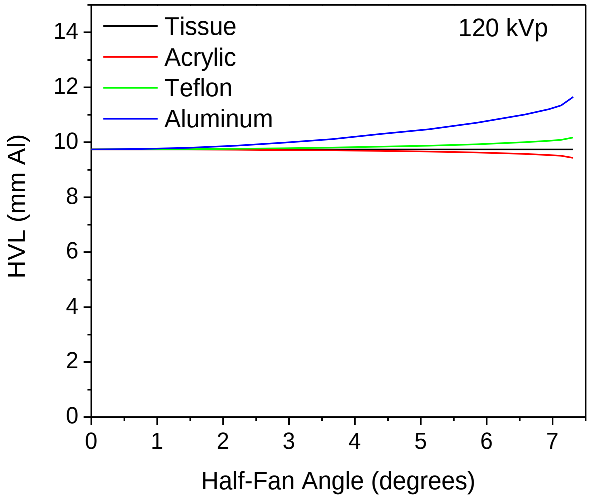

Figure 20. Beam hardening is shown in mm aluminum equivalent HVL versus angle from central axis for filters made from soft-tissue, acrylic, teflon, or aluminum. A tube voltage of 120 kVp was with filters designed for a 14 cm diameter soft (glandular) tissue phantom.

The soft (glandular) tissue filter did not alter the transmitted spectrum with increasing angle, due to the fact that it was made of the same material as the phantom itself; this represented the ideal case. The aluminum filter showed the most hardening with increasing angle due to the fact that its attenuating properties were the most different from tissue out of all the filters simulated. Teflon exhibited the second largest amount of hardening. The adaptive filter made from acrylic softened the beam with increasing angle. This was due to the fact that the effective Z for acrylic was lower than that of soft-tissue. Of the three adaptive filter materials, acrylic exhibited the least variation in beam hardening across the detector field of view. This makes acrylic the best choice for adaptive filter material because variations in the spectral content across the phantom will deteriorate image quality. With this deterioration, the results of energy weighting and material decomposition would be compromised.

Adaptive filters made from acrylic, teflon, and aluminum simulated at 120 kVp tube voltage had beam flatness assessed for 40 kVp, 60 kVp, and 90 kVp tube voltages to investigate spectral non-uniformity over the FOV at differing tube voltages (Figures 18 and 20). The results shown in the above figures were simulated for a 100% soft-tissue (glandular) breast phantom, which was the worst case scenario for use with an acrylic filter due to the largest difference between the effective atomic numbers of acrylic and 100% glandular tissue. However, simulating a 100% soft-tissue (glandular) breast was the best case scenario for filters made from teflon and aluminum. Normal breast tissue comprised of 50% adipose and 50% glandular tissue components has an effective atomic number more similar to acrylic and less similar to teflon and aluminum in comparison to a breast composed of 100% glandular tissue. Further, a 100% adipose breast would possess an effective atomic number almost identical to acrylic, while the differences between the effective atomic numbers between the 100% adipose breast and Teflon/aluminum are the highest. Table 3 compares the elemental mass fractions, densities, and effective Z of adipose and glandular tissue, water, acrylic and 2.5 mg/cm^3 iodine solution in water.

Using an adaptive filter made from acrylic, the highest non-uniformity of x-ray intensity across the detector occurred for the 40 kVp tube voltage (Figure 18a). However, for a 14 cm diameter breast, a 40 kVp tube voltage was suboptimal and a higher tube voltage was needed.

Table 3. Elemental mass fractions, densities and effective Z of selected materials.

Adipose Tissue		**Iodine Solution**		**Glandular Tissue**		**Acrylic**		**Liquid Water**	
Mass Fraction		**Mass Fraction**		**Mass Fraction**		**Mass Fraction**		**Mass Fraction**	
H	0.119477	I	0.000507	H	0.104472	H	0.080538	H	0.111894
C	0.637240	H	0.111837	C	0.232190	C	0.599848	O	0.888106
N	0.007970	O	0.887656	N	0.024880	O	0.319614	-	-
O	0.232333	-	-	O	0.630238	-	-	-	-
Na	0.000500	-	-	Na	0.001130	-	-	-	-
Mg	0.000020	-	-	Mg	0.000130	-	-	-	-
P	0.000160	-	-	P	0.001330	-	-	-	-
S	0.000730	-	-	S	0.001990	-	-	-	-
Cl	0.001190	-	-	Cl	0.001340	-	-	-	-
K	0.000320	-	-	K	0.001990	-	-	-	-
Ca	0.000020	-	-	Ca	0.000230	-	-	-	-
Fe	0.000020	-	-	Fe	0.000050	-	-	-	-
Zn	0.000020	-	-	Zn	0.000030	-	-	-	-
Mass Density		**Mass Density**		**Mass Density**		**Mass Density**		**Mass Density**	
ρ =	0.92 g/cm^3	ρ =	4.93 g/cm^3	ρ =	1.00 g/cm^3	ρ =	1.19 g/cm^3	ρ =	1.00 g/cm^3
Effective Z		**Effective Z**		**Effective Z**		**Effective Z**		**Effective Z**	
Z_{EFF} =	6.230	Z_{EFF} =	7.716	Z_{EFF} =	7.223	Z_{EFF} =	6.467	Z_{EFF} =	7.417

3.1.4. Experimental testing of adaptive filter

Figure 21 shows the measured x-ray intensity profiles for the prototype acrylic adaptive filter. The transmitted profile for the filter and phantom combination, shown in Figures 21(a) and 21(c), was compared to the profile transmitted through a uniform 14 cm thick acrylic slab, shown in Figures 21(b) and 21(d). Figures 21(a) and 21(b) show the experimental results for simple photon counting measurements from 26 keV to 120 keV, while the binned profiles are shown in Figure 21(c) and 21(d).

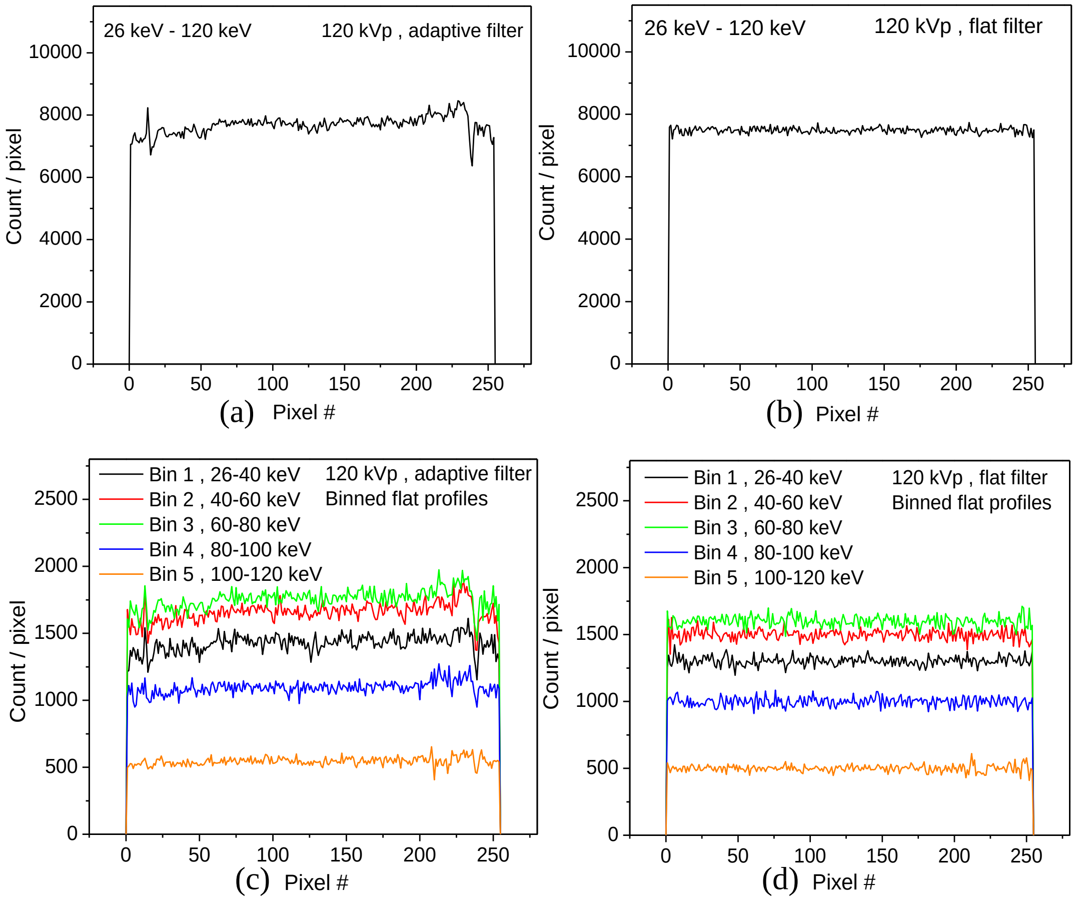

Figure 21. Measured profiles of photon intensity transmitted through the acrylic adaptive filter and 14 cm acrylic phantom, plots (a) and (c), or through a 14 cm thick flat acrylic slab, plots (b) and (d). Profiles were recorded by a 2x256 pixel CZT detector. Plots (a) and (b) show simple photon counting results; plots (c) and (d) show profiles from several energy bins.

Non-uniformities were evident in the profile in Figure 21(a) for the adaptive filter, including spikes near the edges of the profile as well as unevenness and a slight slope across the profile. These were possibly due to machining limitations from the limited number of design calculation points and to incorrect placement of the filter laterally. These non-uniformities carried over to the binned profiles, seen in Figure 21(c). Non-uniformities were not seen with the uniform 14 cm thick acrylic slab, which represents an ideal adaptive filter. The non-uniformities were considered to be minor because the magnitudes were small and they can be cancelled out during CT reconstruction with a normalization procedure similar to the air scans used in commercial CT systems [29].

3.2. CT imaging with adaptive filtration

Figures 22-25 show simple photon counting reconstructed CT images of the simulated breast phantom with contrast elements acquired with an acrylic adaptive filter for tube voltages of 40, 60, 90, and 120 kVp, respectively. In each figure, CT images are shown in (a) – (c) while plots (d) – (f) show horizontal profiles through the center of the images. Also, (a) and (d) correspond to no adaptive filter, (b) and (e) to adaptive filter, and (c) and (f) to adaptive filter with the exposure scaling factor applied to tube output following the methods outlined in section 2.2.2. For all the simulation sets, the relative magnitude of CT noise decreased as the tube voltage increased. This was due to higher photon counts reaching the detector for higher energy beams.

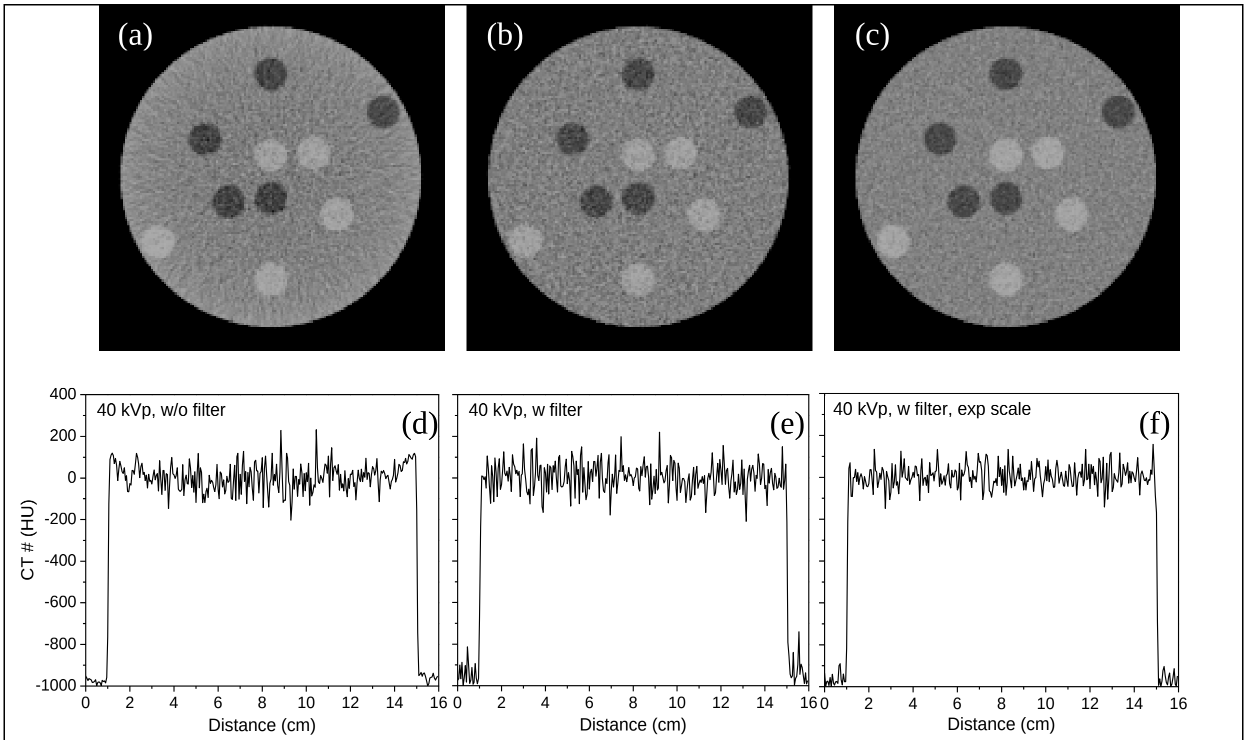

Figure 22. CT images and profiles through the water background acquired at 40 kVp without adaptive filter (a,d), with adaptive filter (b,e), and with adaptive filter with scaled exposure (c,f).

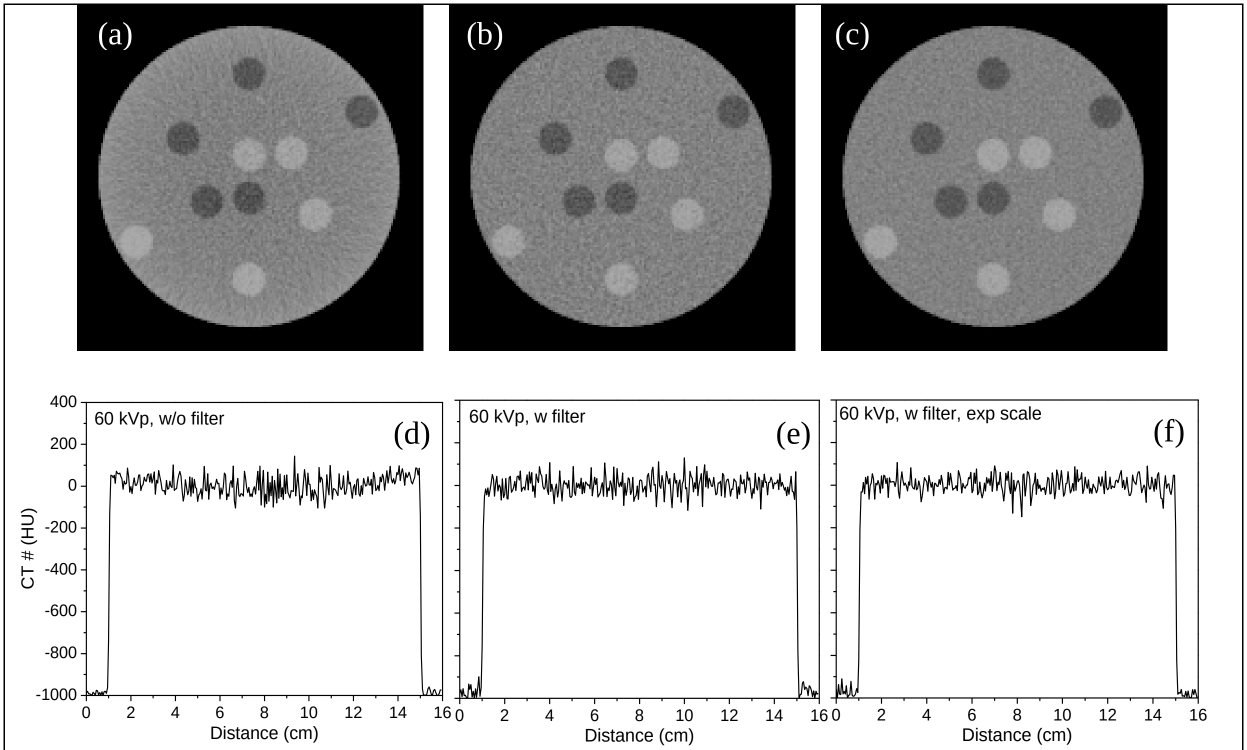

Figure 23. CT images and profiles through the water background acquired at 60 kVp without adaptive filter (a,d), with adaptive filter (b,e), and with adaptive filter with scaled exposure (c,f).

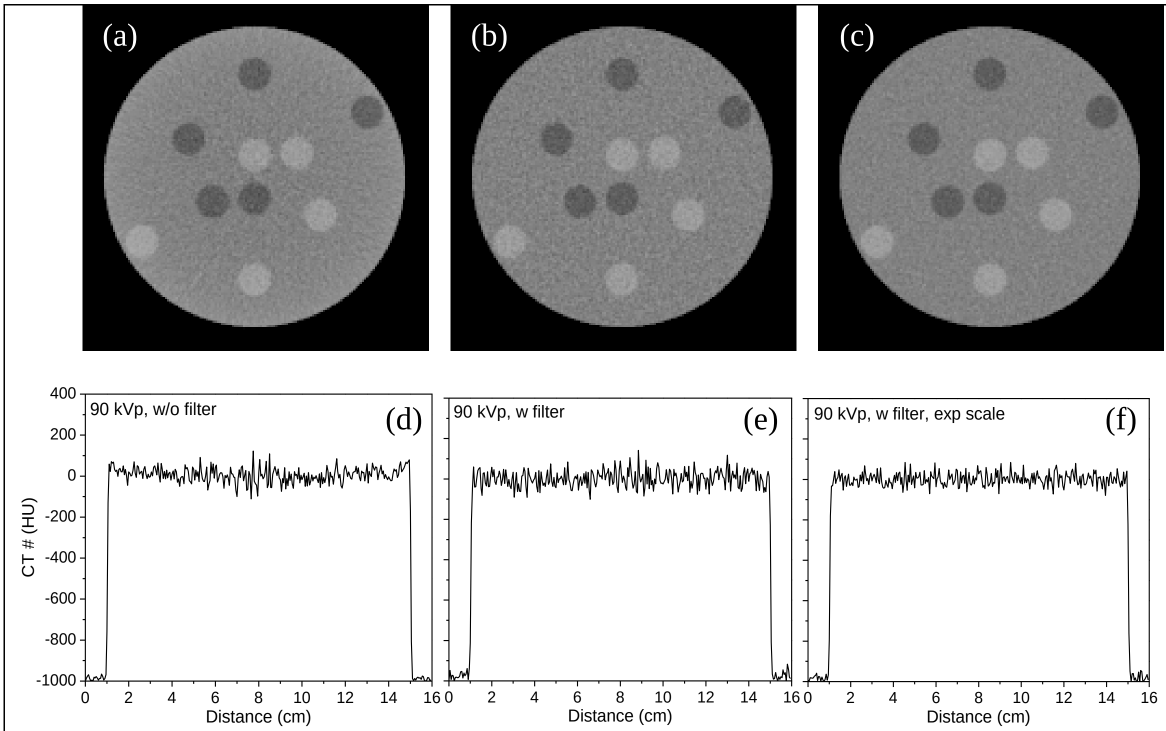

Figure 24. CT images and profiles through the water background acquired at 90 kVp without adaptive filter (a,d), with adaptive filter (b,e), and with adaptive filter and scaled exposure (c,f)

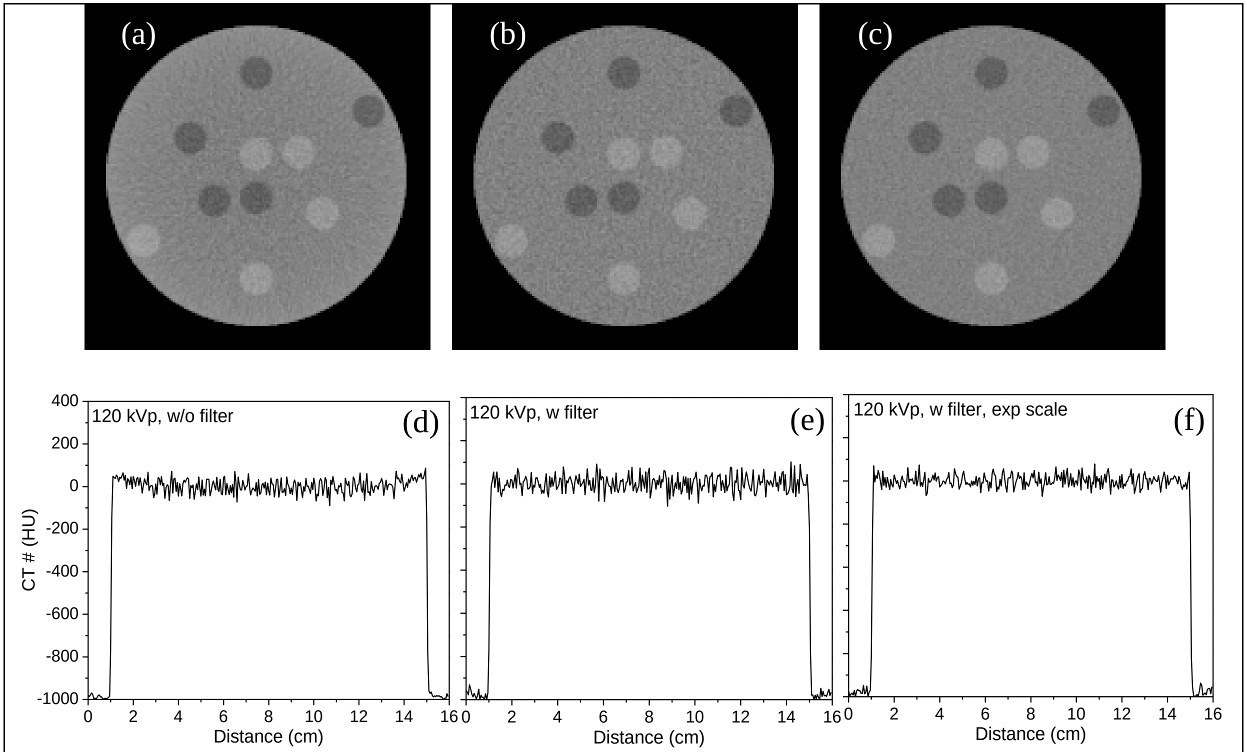

Figure 25. CT images and profiles through the water background acquired at 120 kVp without adaptive filter (a,d), with adaptive filter (b,e), and with adaptive filter with scaled exposure (c,f).

Two artifacts were apparent (Figures 22(d) – 25(d)) for the profiles of the phantom acquired without the adaptive filter. First, a cupping artifact was seen which decreased in magnitude as the tube voltage increased from 40 kVp to 120 kVp. Second, the noise magnitude increased from the periphery to the center of the phantom. This was due to higher numbers of photons reaching the detector at the periphery of the phantom because less attenuating material was in the path of the photons. Introducing the adaptive filter made the noise uniform across the phantom profile, but with a magnitude corresponding to the center of the unfiltered data. The adaptive filter removed the cupping artifact as well. An increased tube output with adaptive filtration reduced the magnitude of noise to a level similar to the magnitude of noise seen at the periphery of the phantom with no adaptive filter.

The CT number distribution, represented in HU, is shown in Figure 26 for the 3 simulation sets for 40, 60, 90, and 120 kVp beams. For all sets at all tube voltages, the mean value of the background at 3.5 cm radial distance from the center of the phantom was normalized to zero HU. Without the adaptive filter, CT number increased from the center of the phantom towards the periphery, which is the cupping artifact. The lower mean energy of the photons arriving at the detector along the periphery of the phantom resulted in a higher apparent mean attenuation coefficient. The cupping artifact was largest for the 40 kVp beam with a magnitude of 40 HU, and decreased as the tube voltage increased, becoming 27 HU at 120 kVp tube voltage. With the adaptive filter, the CT number distribution became flat with radial distance. The was due to the filter compensating for less attenuating material at the phantom periphery, eliminating the falloff with increasing radial distance.

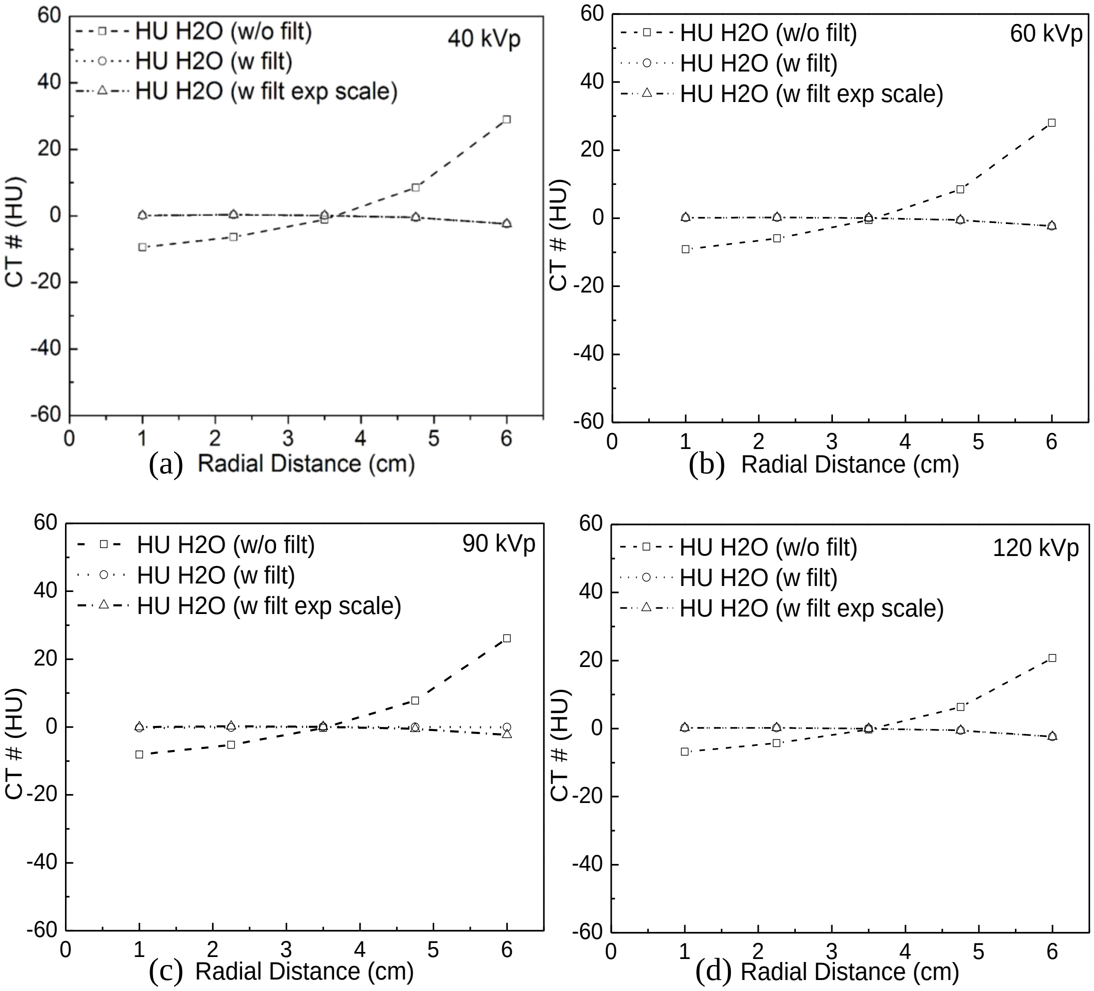

Figure 26. CT number distributions without the adaptive filter (w/o filt), with the adaptive filter (w filt) and with the adaptive filter and the exposure scaling factor applied (w filt exp scale) at (a) 40 kVp, (b) 60 kVp, (c) 90 kVp, and (d) 120 kVp.

Figure 27 shows the mean magnitude of noise in CT ionization chamber versus radial distance from the center of the phantom for simple photon counting reconstructed images. The noise magnitude decreased as the tube voltage increased. Without adaptive filtration, the mean magnitude of noise decreased from the center of the phantom toward the periphery. The magnitude of noise was uniform with the adaptive filter, but the mean value was higher than without the adaptive filter. The adaptive filter with increased exposure showed a uniform but decreased magnitude of noise due to the scaled up tube output.

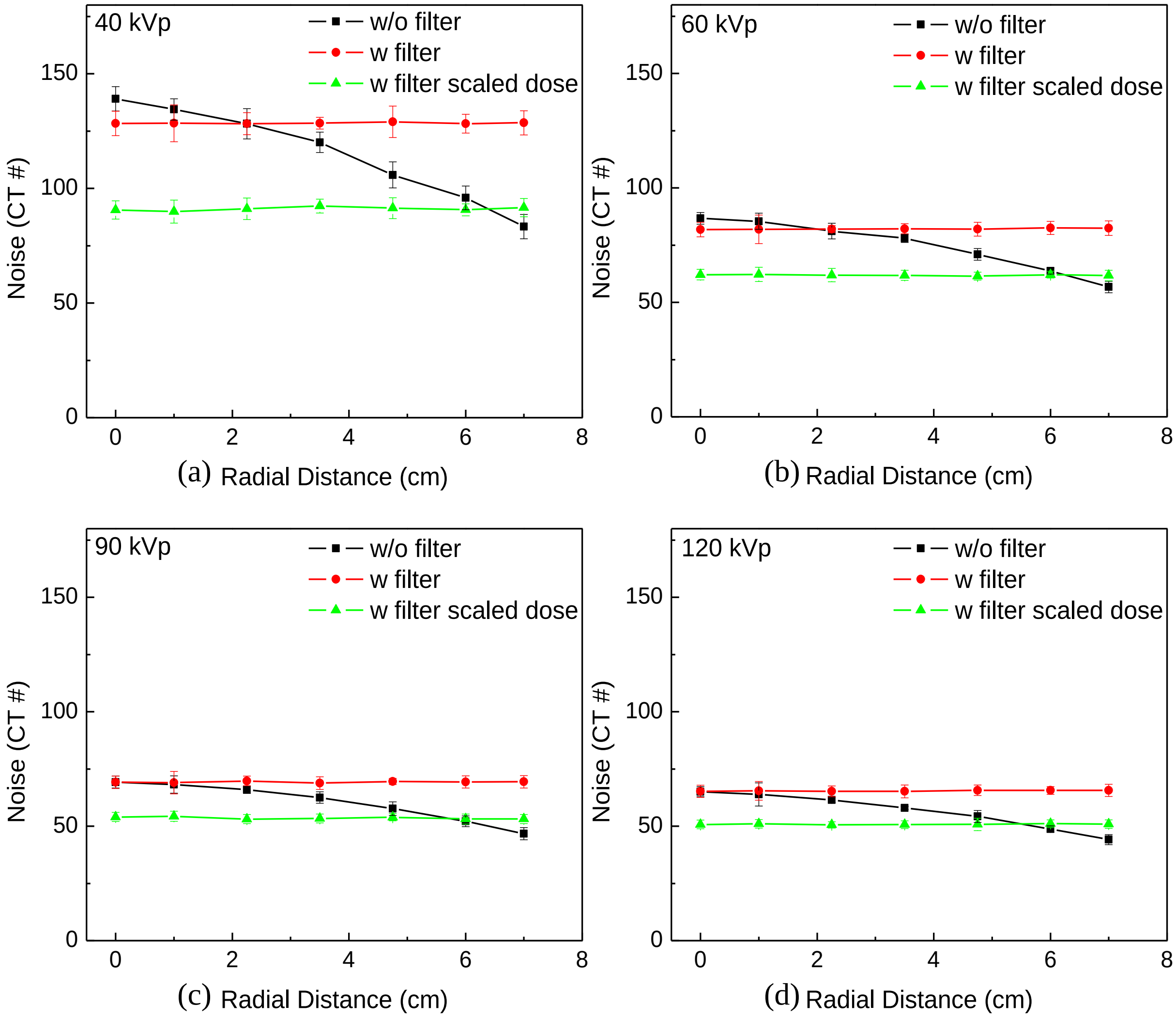

Figure 27. Noise in CT number versus radial distance shown at 40 kVp (a), 60 kVp (b), 90 kVp (c), and 120 kVp (d) for simple photon counting. The points at 0 cm and 7 cm radial distance were extrapolated from the other points measured for the curve.

Although the same ESE was used for all tube voltages, the magnitude of noise consistently decreased when the tube voltage increased. Higher energy x-rays passed through the phantom and filter more easily than lower energy x-rays, and provided better photon statistics and hence lower noise. This advantage of higher energy photons was offset by an inherently lower subject contrast that decreases the overall CNR.

Figure 28 shows the CNR of contrast elements versus tube voltage for simple photon counting CT imaging. Figures 28(a) and 28(b) correspond to adipose contrast elements, while Figures 28(c) and 28(d) show results for the phantom containing iodine contrast elements. Figures 28(a) and 28(c) show the results without the adaptive filter, and the Figures 28(b) and 28(d) each show the results for adaptive filtration with and without the exposure scaling factor applied. The 60 kVp tube voltage provided the highest CNR for all simulation sets and contrast element positions. For all tube voltages, introducing the adaptive filter made CNR more consistent across contrast element positions. The adaptive filter with scaled exposure resulted in CNR magnitudes for all contrast element positions comparable to the CNR of the unfiltered peripheral contrast elements.

Figures 29 and 30 show the CNR distributions for iodine and adipose contrast elements, respectively, plotted against radial distance for each tube voltage. Without the adaptive filter, the CNR increased from the center of the phantom towards the periphery. Introducing the adaptive filter resulted in a more uniform CNR over the profile of the phantom; however, the mean value of CNR was similar to the mean value of CNR without the adaptive filter at the center of the phantom. Utilizing the adaptive filter and increasing the tube output resulted in a uniform CNR distribution that had a mean value similar to that at the phantom periphery without the adaptive filter. CNR improved with the increased tube output mainly through reduction in noise magnitude, and not through an increase in contrast. Contrast, instead, remained relatively constant for all contrast element types and positions when using the adaptive filter.

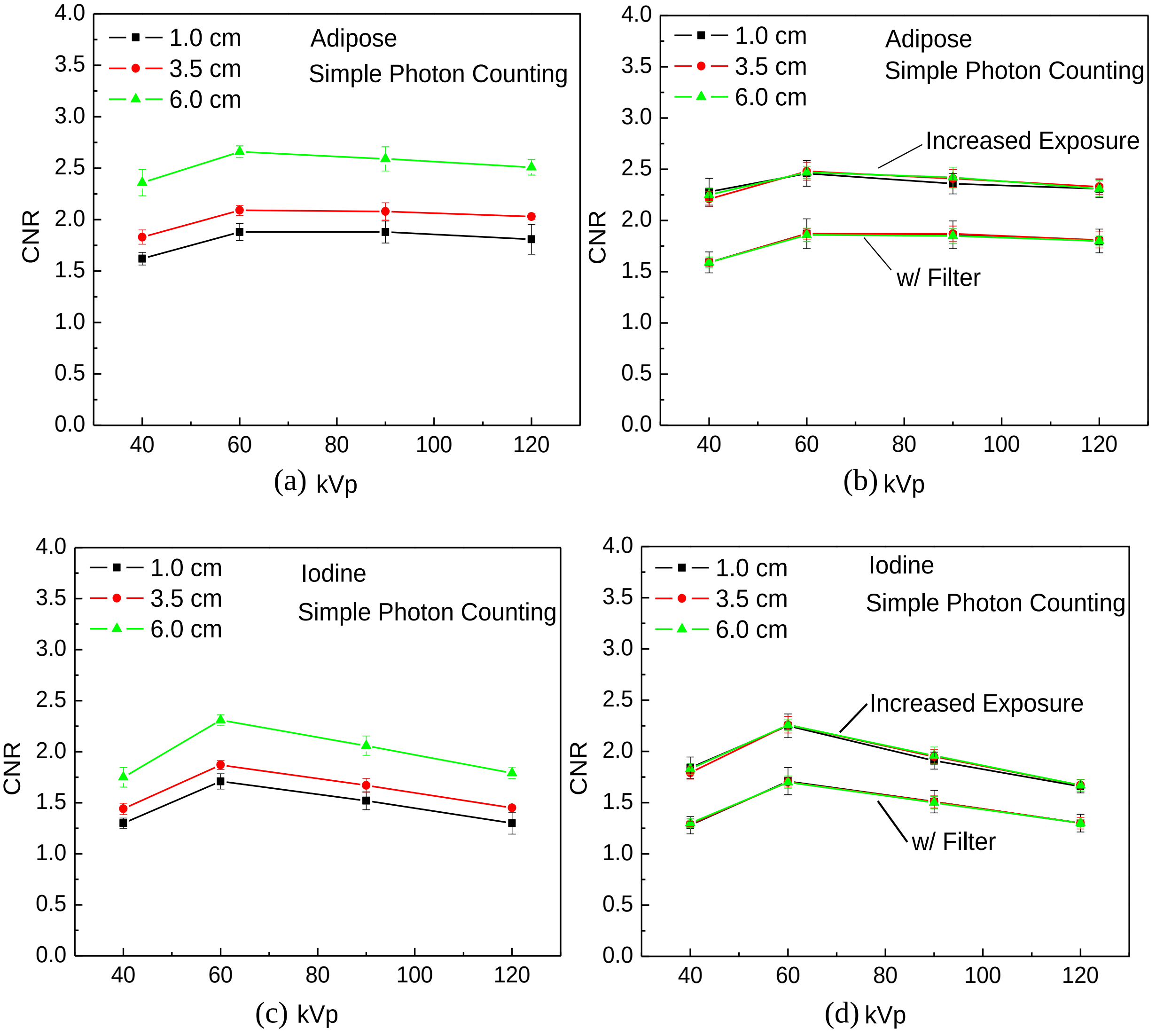

Figure 28. CNR of contrast elements in CT images acquired at 40-120 kVp tube voltages, acquired without (a, b) and with (c, d) adaptive filtration with or without the exposure scaling factor applied.

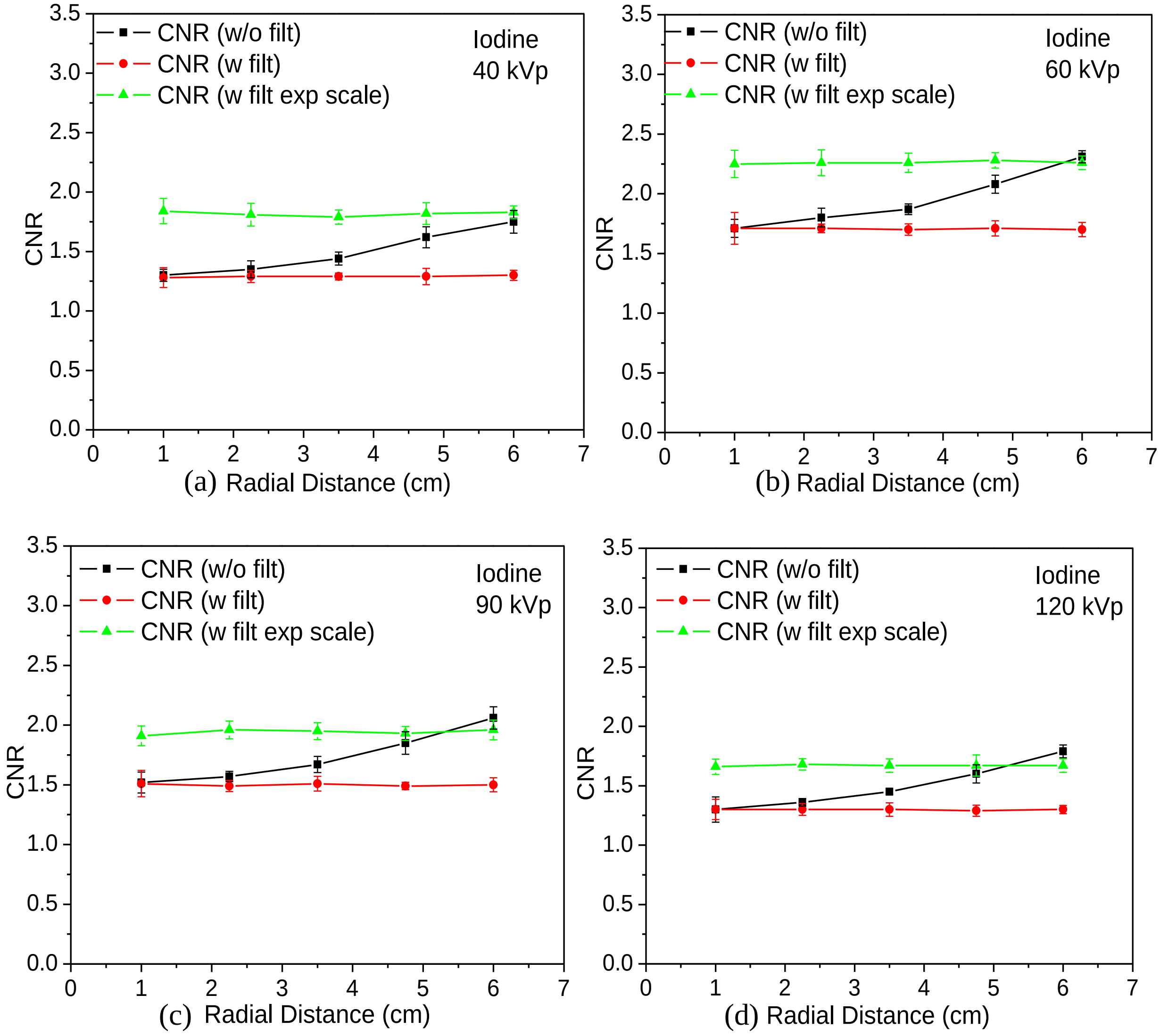

Figure 29. Simple photon counting results showing the iodine contrast element CNR with error bars versus radial distance for 40 kVp (a), 60 kVp (b), 90 kVp (c), and 120 kVp (d) tube voltages.

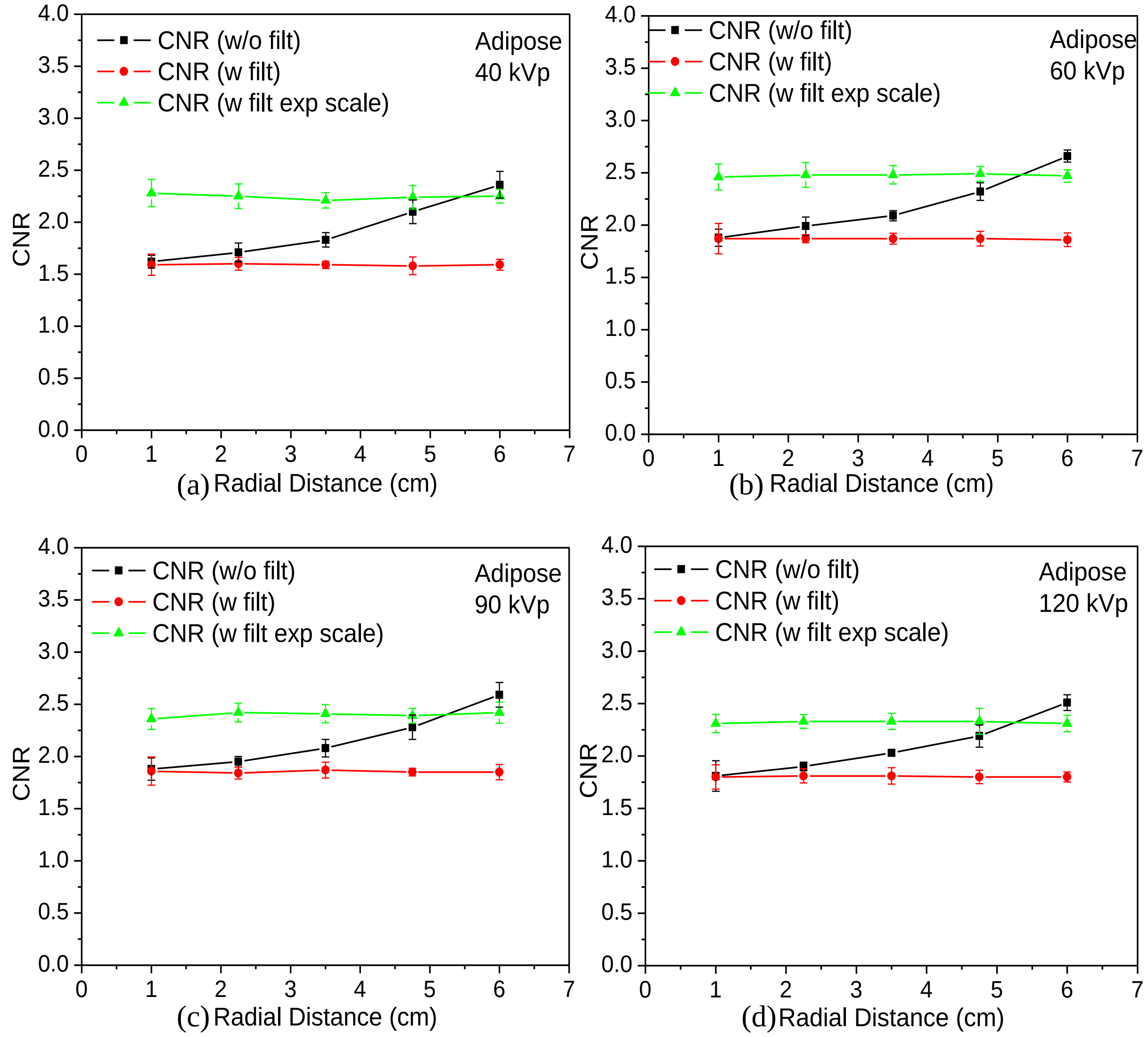

Figure 30. Simple photon counting results showing adipose CNR with error bars versus radial distance for 40 kVp (a), 60 kVp (b), 90 kVp (c), and 120 kVp (d) tube voltages.

3.3. Energy weighting and material decomposition

Figures 31 and 32 compare simple photon counting CNR and energy weighting CNR, plotted versus tube voltage, for iodine and adipose contrast elements at three radial distances. The plots also compare the CNR achieved with and without adaptive filtration. Energy weighting improved CNR for each contrast element type and position. The 90 kVp beam showed the most improvement through the use of energy weighting for iodine and adipose contrast elements for all simulation sets.

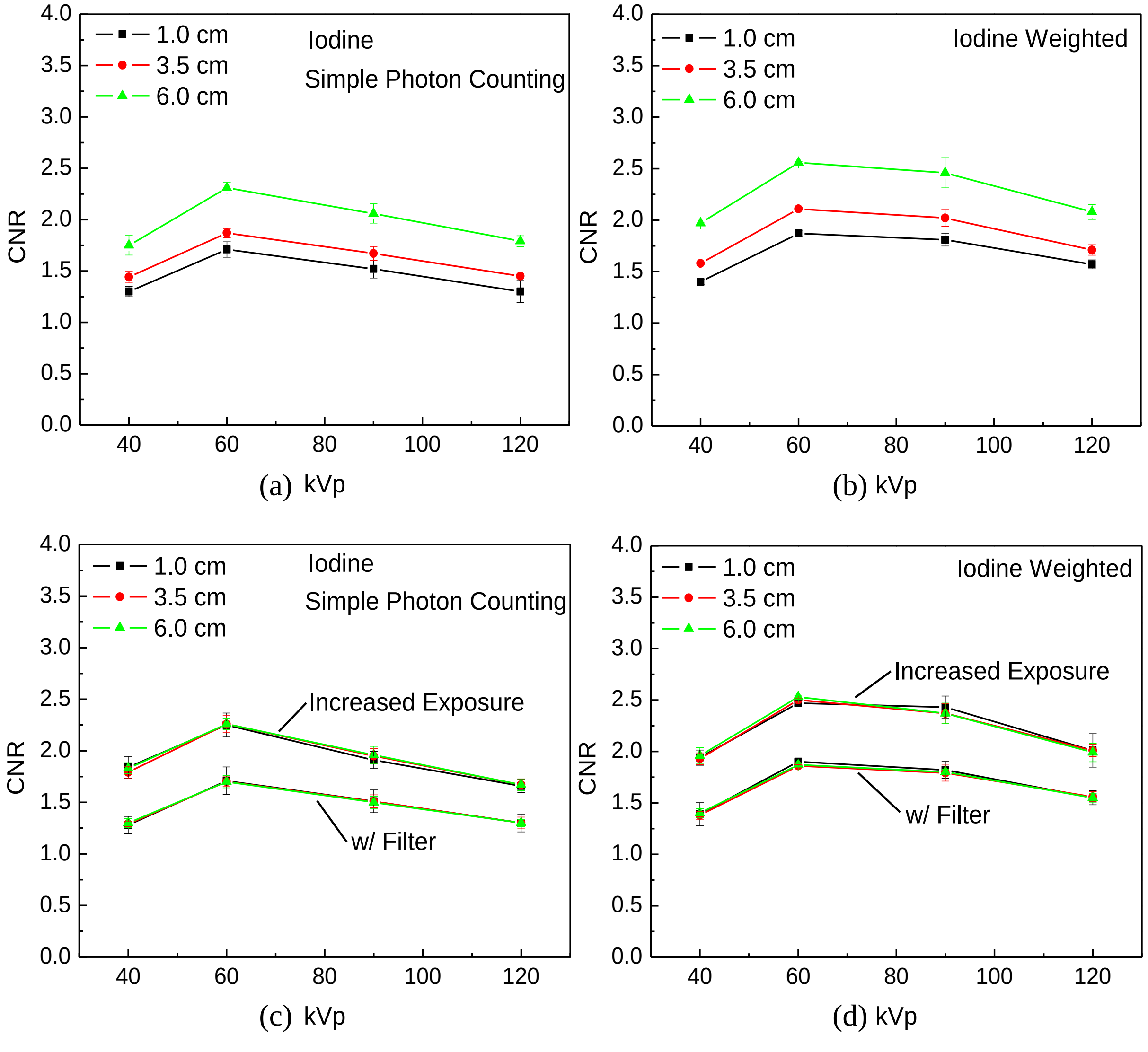

Figure 31. CNR of iodine contrast elements in CT images acquired at 40-120 kVp tube voltages, acquired without (a, b) and with (c, d) adaptive filtration, and without (a, c) and with (b, d) optimized energy weighting.

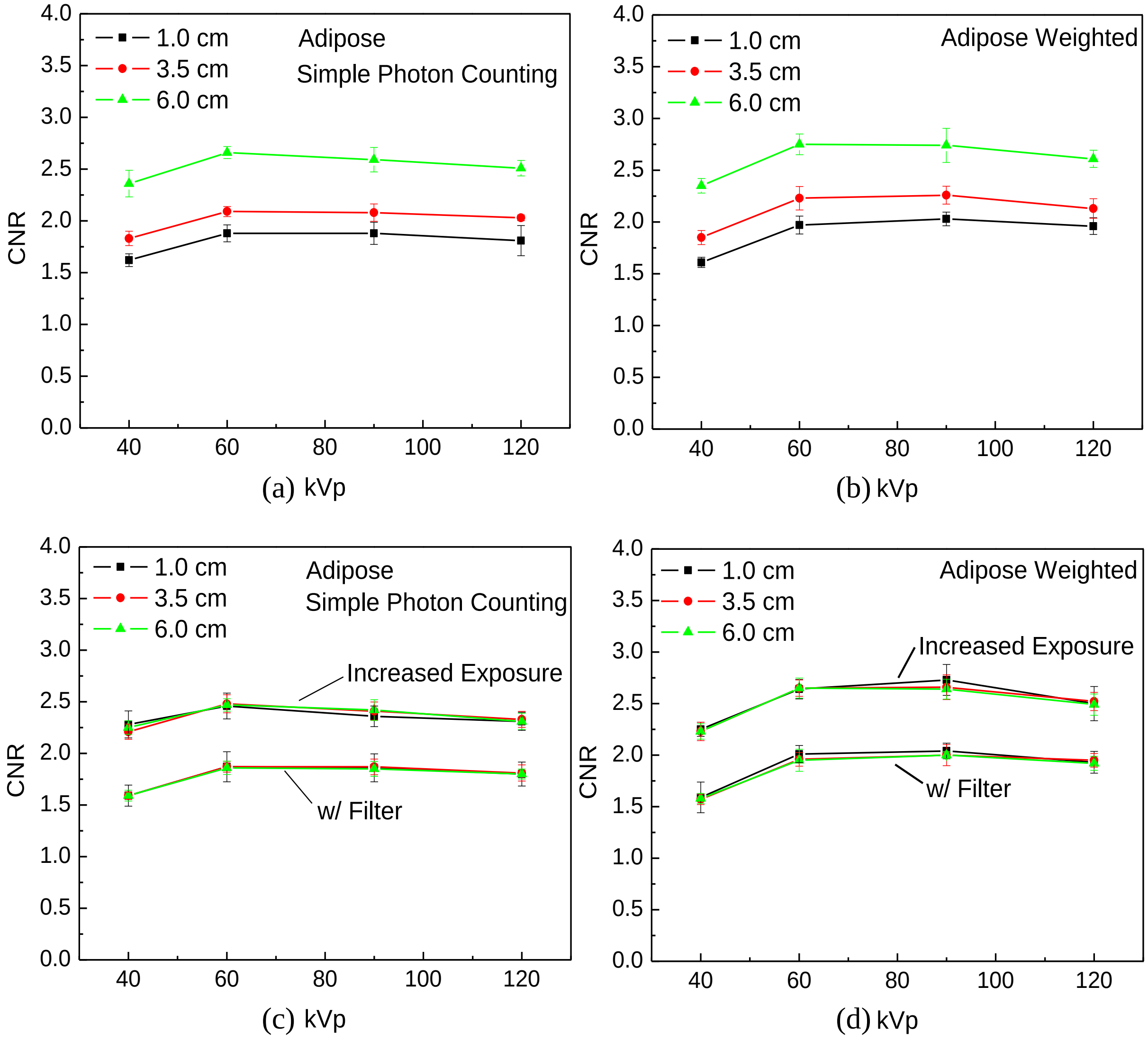

Figure 32. CNR of adipose contrast elements in CT images acquired at 40-120 kVp tube voltages, acquired without (a, b) and with (c, d) adaptive filtration, and without (a, c) and with (b, d) optimized energy weighting.

Figures 33 through 36 show the material decomposed images for iodine and adipose for each tube voltage, respectively. The material decomposition method required the subtraction of one noisy image from another, resulting in a final image that had small signal values, and the noise of each binned image added in quadrature. Therefore, the small signal values combined with even larger noise values made the images less sharp; however, the reconstructed images clearly showed one contrast element had been visibly removed from the image sets. Material decomposition has important clinical applications for characterizing types of tissues in vivo. For instance, material decomposition facilitates quantification of iodine uptake or other contrast over complex soft-tissue background.

Figures 37 through 40 show the overall behavior of CNR in material decomposed CT images acquired with and without the adaptive filter. The results followed roughly the same behavior as the simple photon counting case, with the exception that the magnitude of noise was greatly increased for all contrast element types and positions. The CNR values exhibited relatively large standard deviations, an inherent limitation of dual energy subtracted images. Despite the magnitude of standard deviation, the trends in the mean values of CNR were clearly seen; images acquired without adaptive filter showed a radial dependence of CNR while this dependence was reduced when the adaptive filter was used.

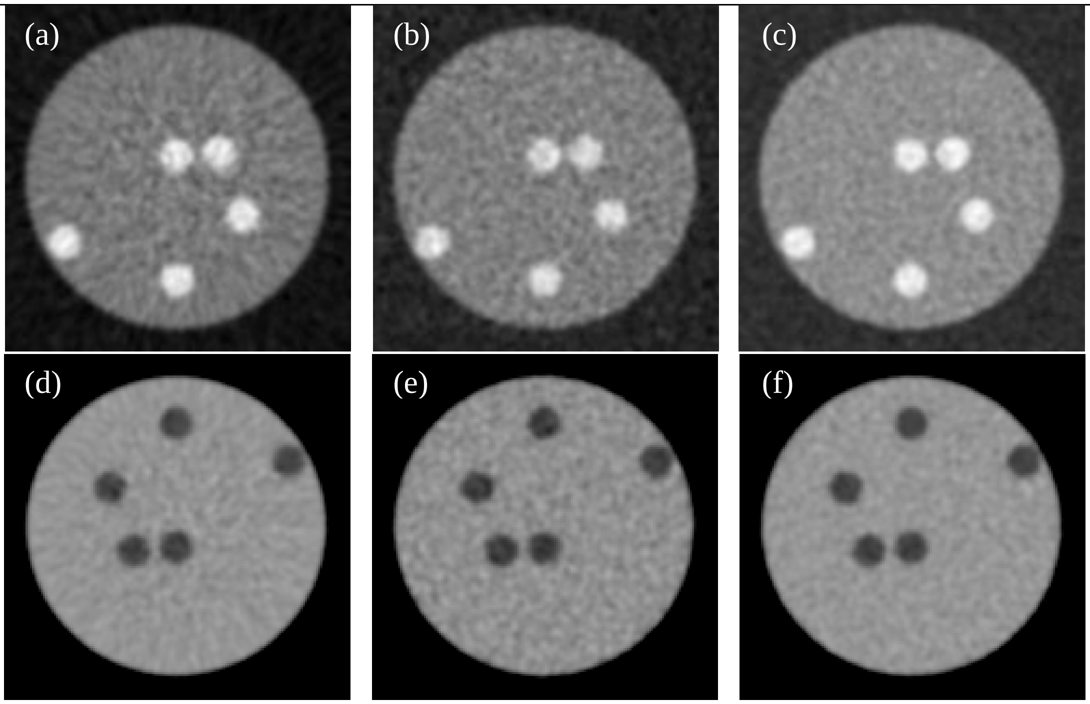

Figure 33. Material-decomposed images acquired at 40 kVp without adaptive filter (left column), with adaptive filter (middle column), and with adaptive filter and scaled exposure (right column). Top row: adipose cancelled images; bottom row: iodine cancelled images.

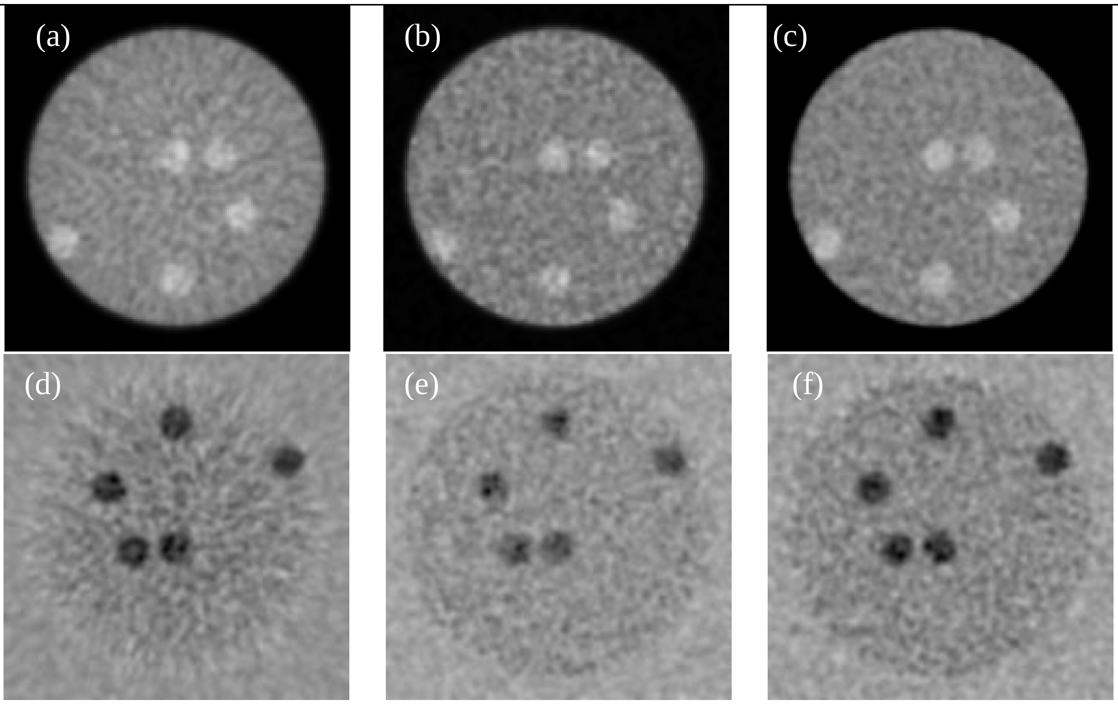

Figure 34. Material-decomposed images acquired at 60 kVp without adaptive filter (left column), with adaptive filter (middle column), and with adaptive filter and scaled exposure (right column). Top row: adipose cancelled images; bottom row: iodine cancelled images.

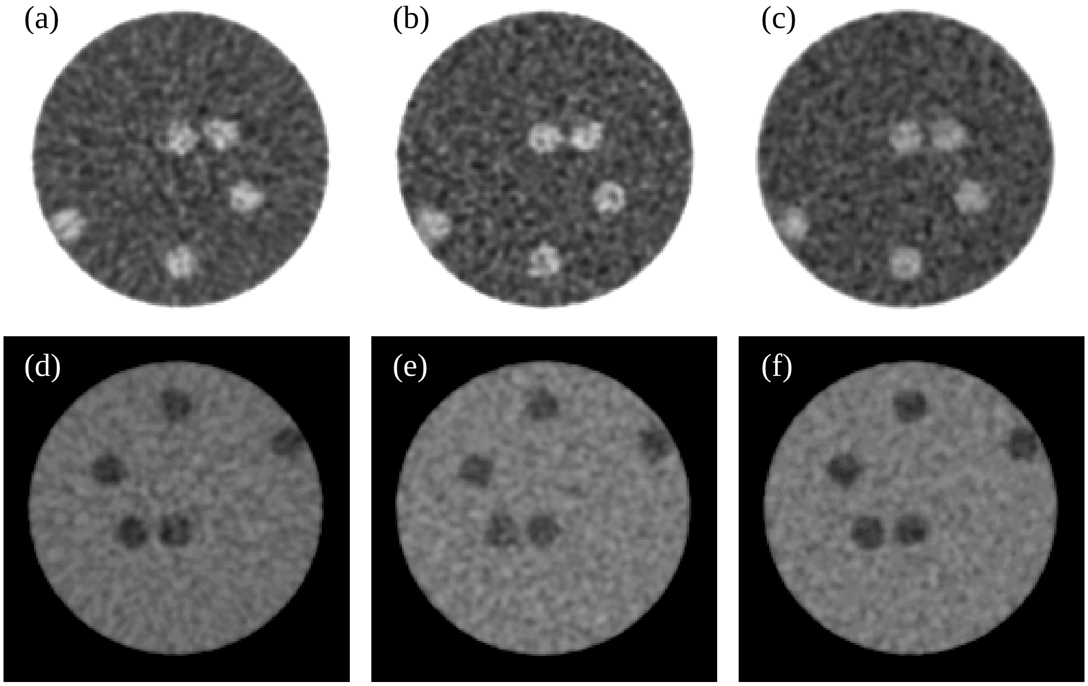

Figure 35. Material-decomposed images acquired at 90 kVp without adaptive filter (left column), with adaptive filter (middle column), and with adaptive filter and scaled exposure (right column). Top row: adipose cancelled images; bottom row: iodine cancelled images.

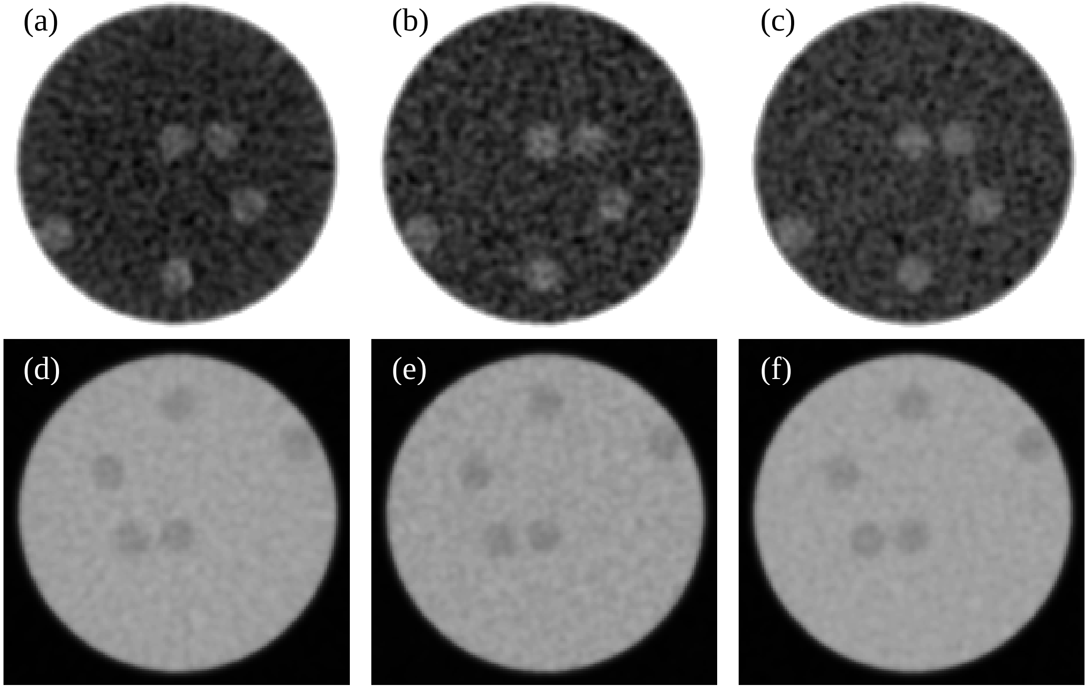

Figure 36. Material-decomposed images acquired at 120 kVp without adaptive filter (left column), with adaptive filter (middle column), and with adaptive filter and scaled exposure (right column). Top row: adipose cancelled images; bottom row: iodine cancelled images.

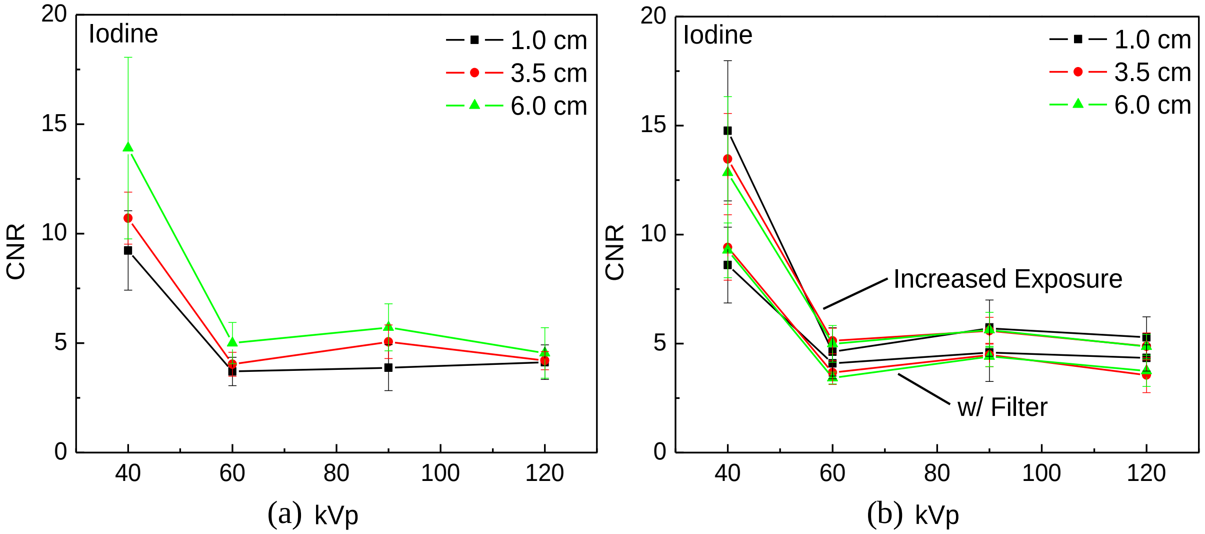

(a) (b)

Figure 37. CNR distributions of iodine contrast elements in adipose cancelled images versus kVp (a) without adaptive filter; (b) with adaptive filter or with the adaptive filter and scaled exposure.

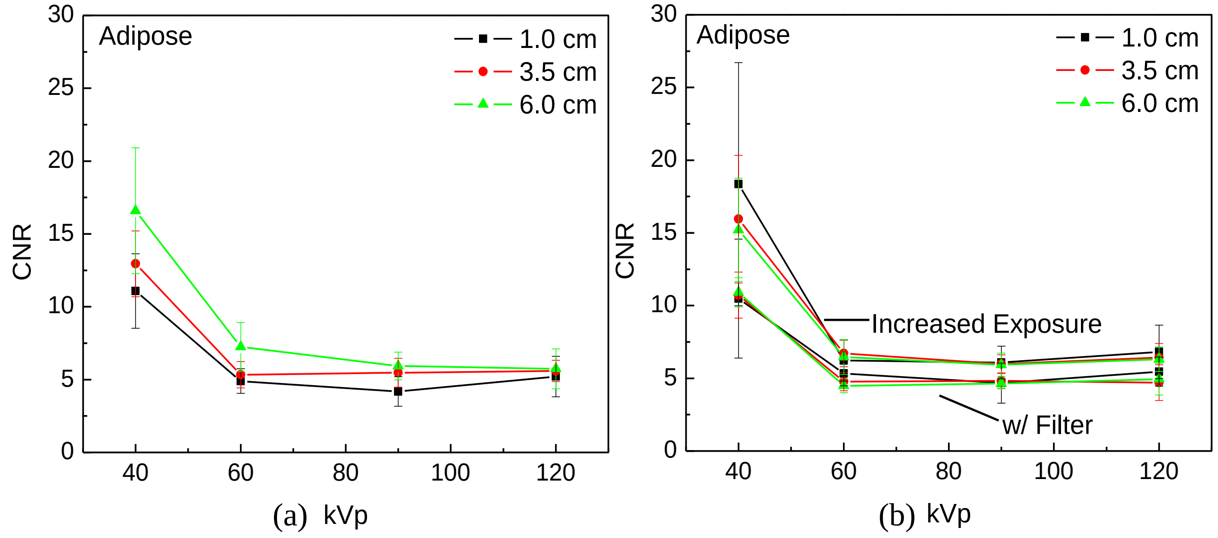

Figure 38. CNR distributions of adipose contrast elements in iodine cancelled images versus kVp (a) without adaptive filter, (b) with adaptive filter or with the adaptive filter and scaled exposure.

3.4. Breast dose measurements

Figure 41 shows 2D maps of dose deposited in a 14 cm diameter acrylic phantom for scans without the acrylic adaptive filter, with the adaptive filter, and with the adaptive filter and the dose increased using the dose increase scaling factor shown in Figure 43. Results are shown for 40 kVp, 60 kVp, 90 kVp, and 120 kVp beams. Absorbed dose was recorded in units of mGy. For scans without the adaptive filter, dose was higher along the periphery of the phantom. Introducing the adaptive filter lowered the mean dose to the phantom, and also deposited the dose more uniformly across the phantom for 40 kVp and 60 kVp beams. The dose deposited to the central parts of the phantom was higher than the periphery of the phantom for 90 kVp and 120 kVp beams. Increasing the tube output with the adaptive filter made the mean dose deposited equal to that without the filter, while the nature of the relative dose distribution does not change compared to that with the adaptive filter without scaled up dose.

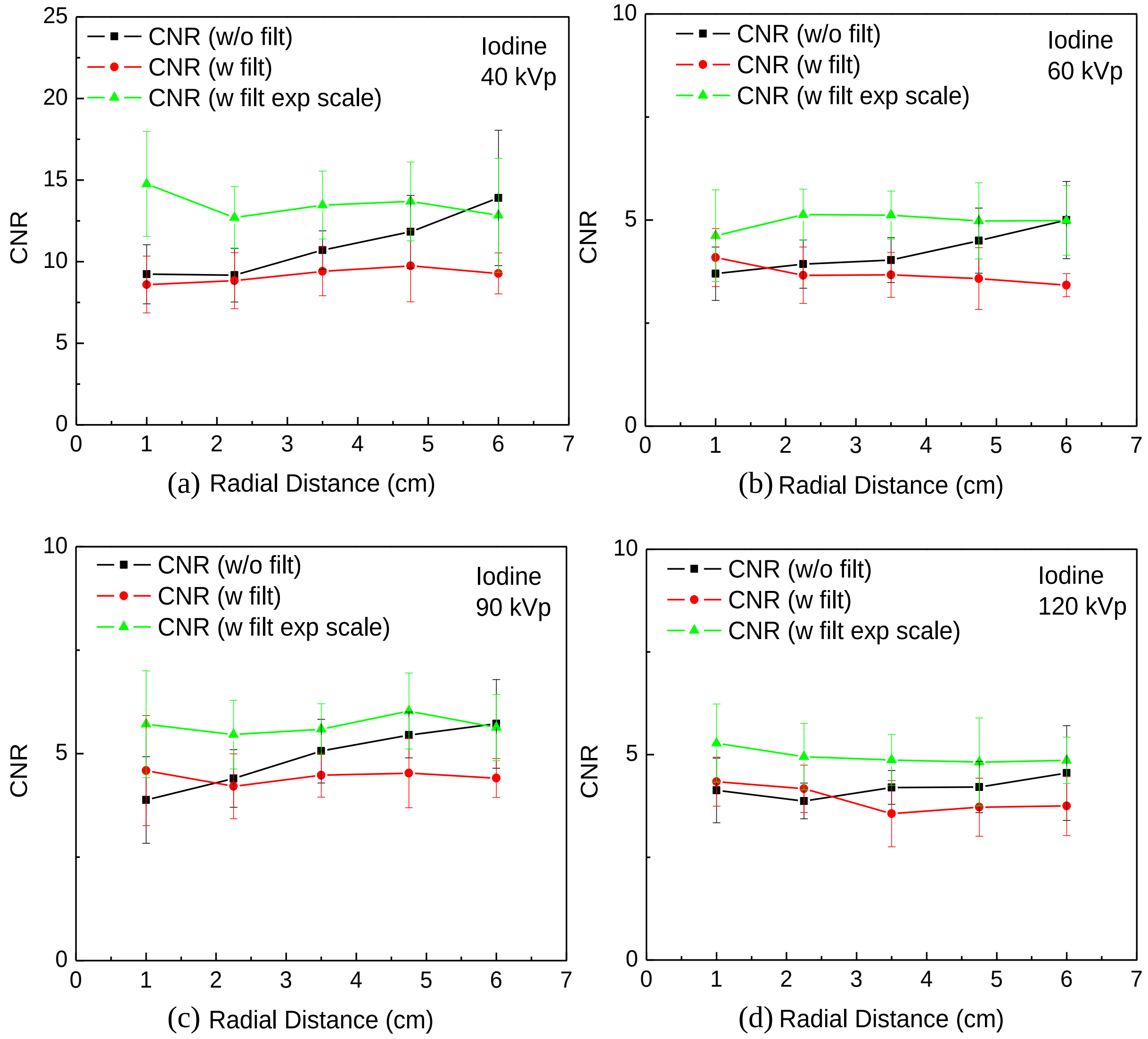

Figure 39. CNR versus radial distance of iodine contrast elements for adipose subtracted images at each tube voltage.

Figure 42 shows the dose distribution versus radial distance from the center of the phantom for the three situations: without the adaptive filter, with the adaptive filter, and with the adaptive filter and scaled output. An associated error was measured as 5% of the measured dose for a particular point. Second order polynomials were fitted to the data and used to extrapolate to a point at the edge of the phantom.

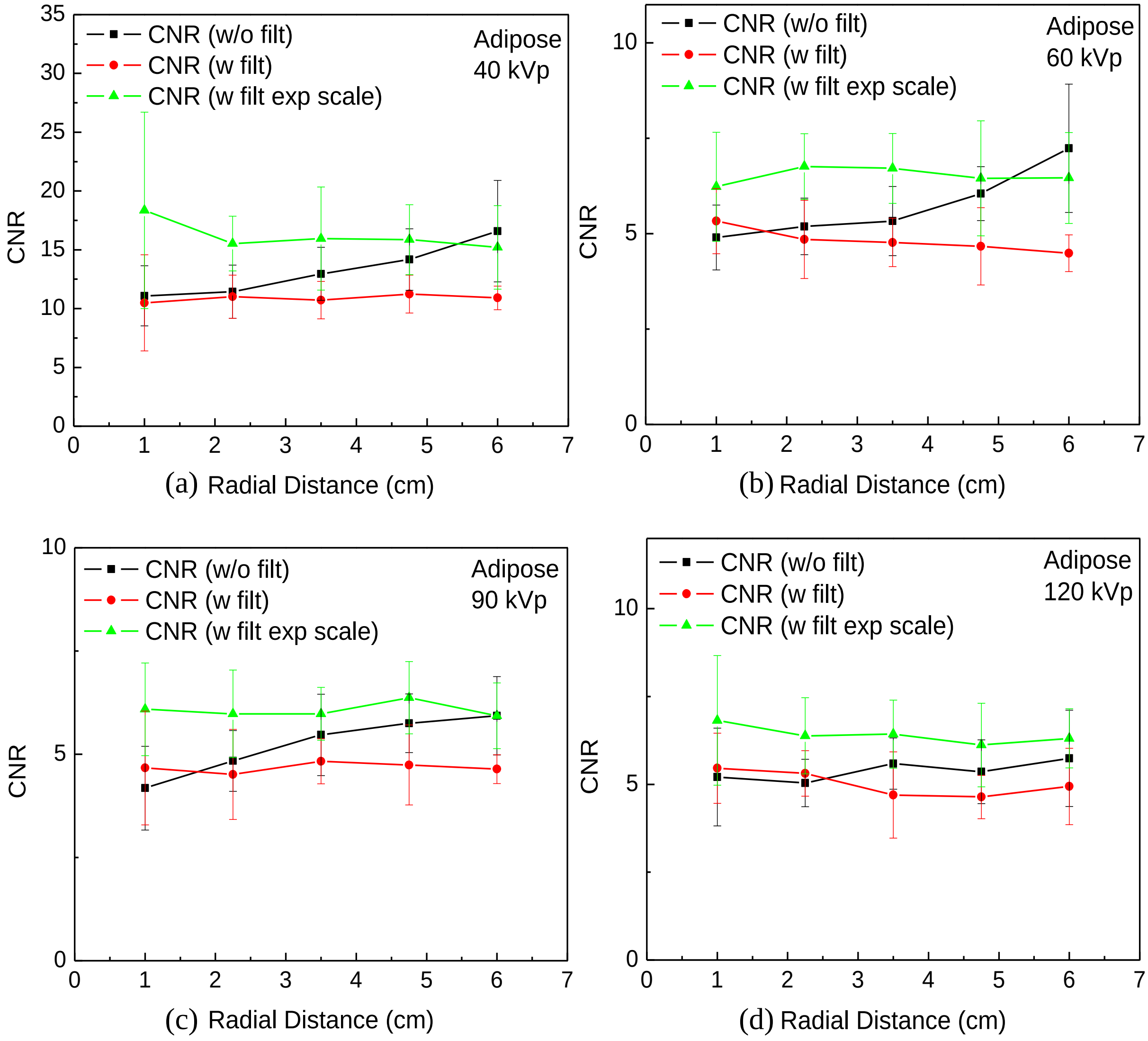

Figure 40. CNR versus radial distance of adipose contrast elements for iodine subtracted images at each tube voltage.

In the simulation studies, the tube current was increased by an exposure scaling factor with the adaptive filter to compensate for beam attenuation by the adaptive filter and to return the mean ESE to the unfiltered level. However, the same mean ESE does not result in the same mean dose. Alternatively, a dose increase scaling factor could be defined to provide the same mean dose with the adaptive filter as the mean dose without the adaptive filter. Analogous to the exposure increase scaling factor, the dose increase scaling factor was defined as the ratio of the mean dose without the adaptive filter to the mean dose with adaptive filter. Figure 43 compares the exposure and dose scaling factors versus tube voltage. As seen from the figure, these two factors substantially differ one from another, depending on tube voltage.

Without adaptive filtration, the volume distribution of breast dose was expected to be non-uniform. Higher deposited dose was expected around the periphery of the breast compared to its central parts because more low energy x-rays are absorbed in the periphery of the breast. This effect was expected at all tube voltages, while its magnitude should decrease as tube voltages increase due to increased penetrating ability of the x-rays at higher energy. Adaptive filtration was expected to provide a more uniform dose distribution over the volume of the breast, due to a decreased amount of x-rays along the periphery of the breast. Results, however, showed that uniformity of the volume distribution of dose with adaptive filtration depended heavily on the tube voltage used, as shown in Figures 41 and 42. At tube voltages of 90 kVp and 120 kVp, the volume distribution of breast dose using adaptive filtration had similar non-uniformity as the scans obtained without the adaptive filter. The magnitude of dose non-uniformity, however, was reversed compared to scans made without adaptive filtration. At tube voltages of 40 kVp and 60 kVp, the dose distribution was substantially more uniform. The non-uniformity in volume distribution of dose for 90 kVp and 120 kVp scans might have been attributed to over-attenuation of the x-ray beam towards the periphery of the breast. More optimal attenuation occurred at 40 kVP and 60 kVp tube voltages for more uniform dose over the breast volume.

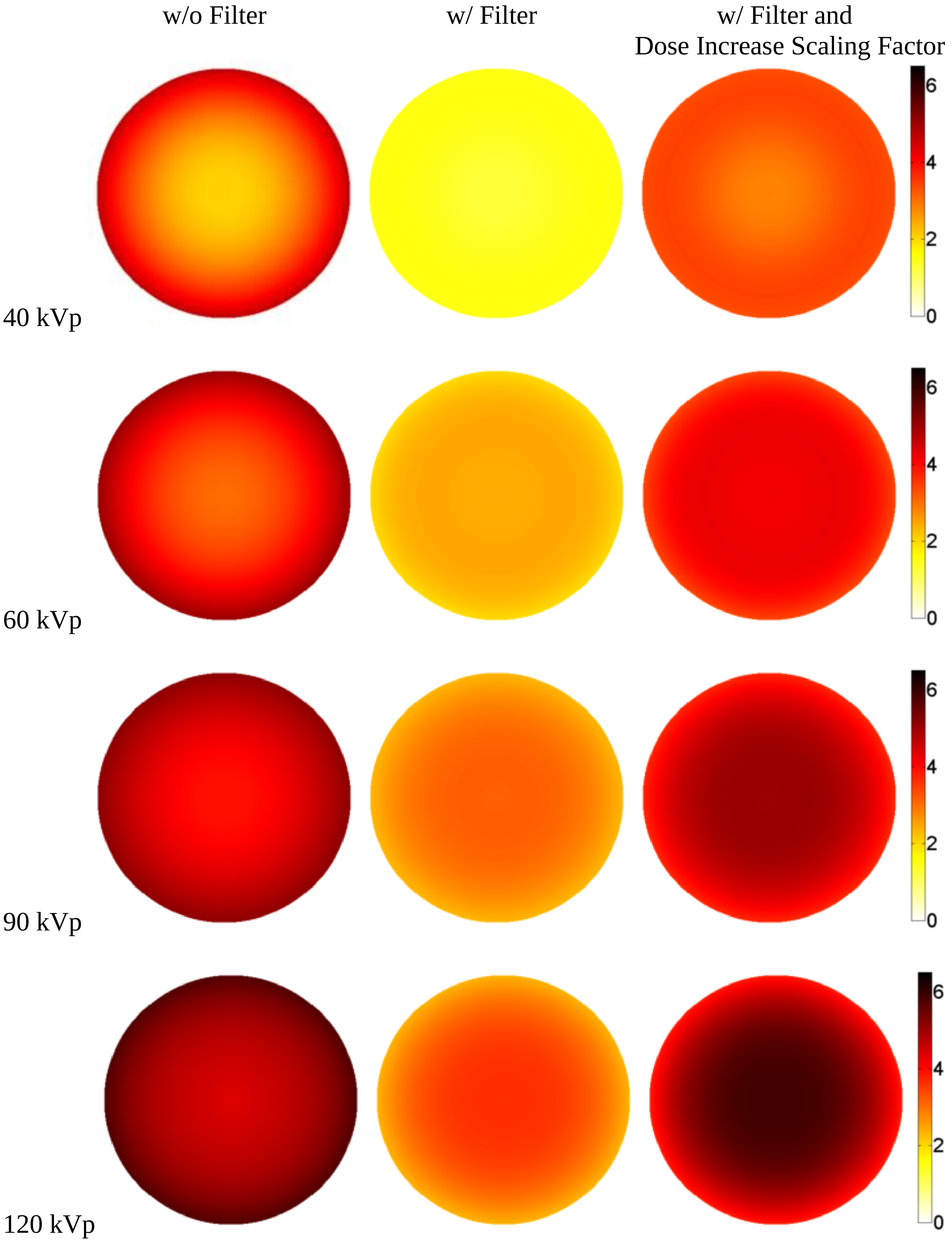

Figure 41. 2D color maps of dose distributions in the breast.

The adaptive filter used for dose measurement was fabricated from acrylic, a tissue-like material, and was designed to provide a uniform x-ray exposure at the detector surface at 120 kVp. It appeared, however, that an adaptive filter optimally designed for CT image quality at one tube voltage was suboptimal for dose uniformity at other tube voltages.

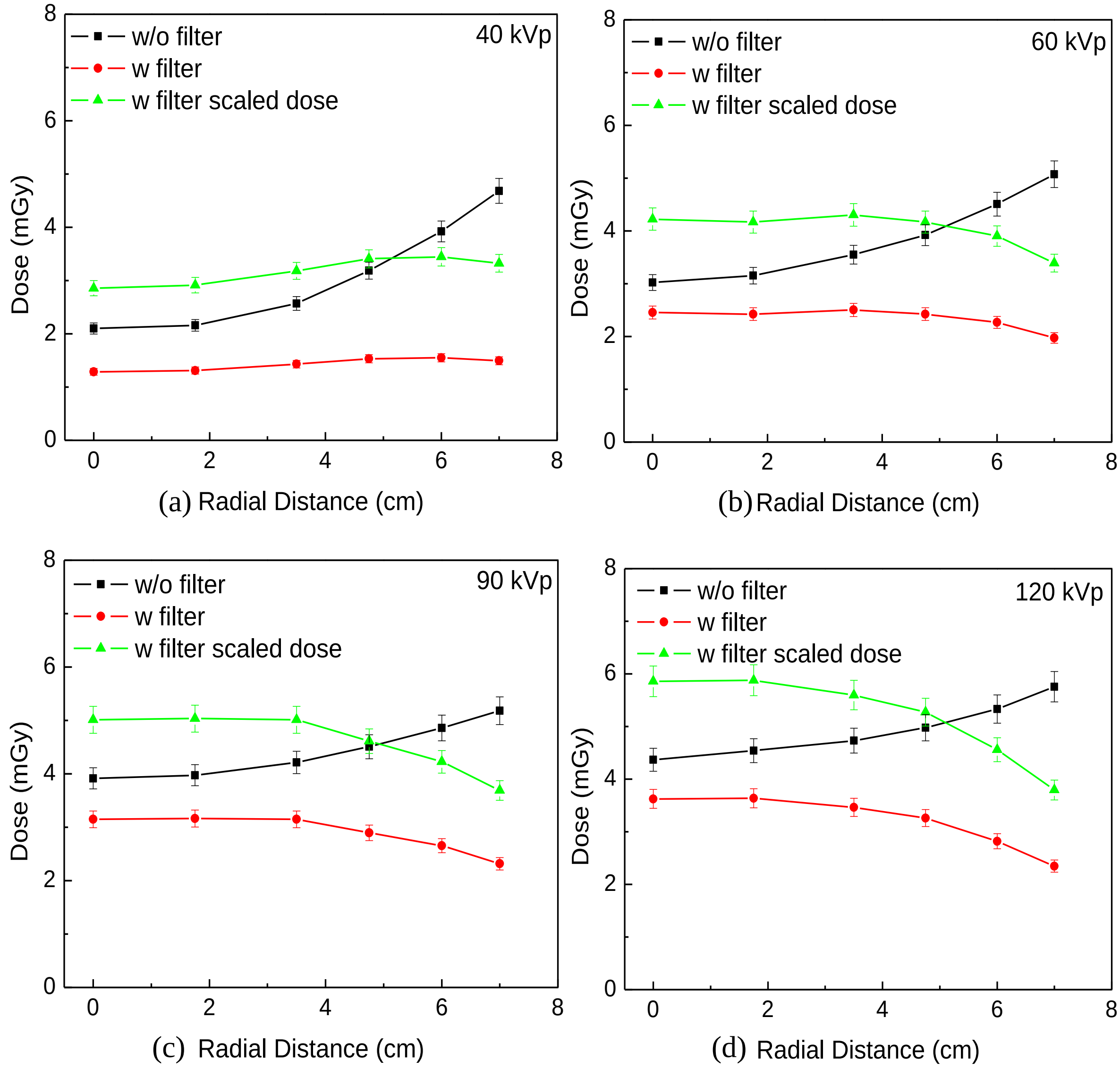

Figure 42. Radial distributions of the breast dose measured at 40 kVp (a), 60 kVp (b), 90 kVp (c), and 120 kVp (d) tube voltages. The dose distributions are presented for the cases without an adaptive filter, with an adaptive filter, and with an adaptive filter and with dose increased by the dose increase scaling factor to account partial absorption of the x-rays by the adaptive filter.

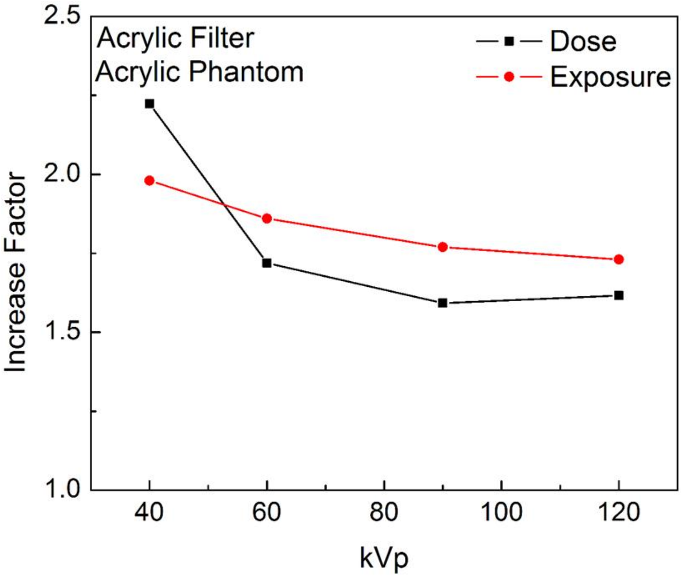

Figure 43. Exposure and dose increase factors versus tube voltage. The tube current is increased by these factors when adaptive filter is used, to compensate beam attenuation by adaptive filter. The dose increase factor is used to provide same mean dose with the adaptive filter as the mean dose without the adaptive filter. Exposure increase factor is used to provide same mean ESE with the adaptive filter as mean ESE without the adaptive filter.

The mean absorbed dose is plotted versus tube voltage in Figure 44**.** Using the adaptive filter resulted in the lowest mean dose for all tube voltages. The mean dose when using the exposure-based scaling factors resulted in a slightly lower mean dose at 40 kVp but higher mean doses at the higher tube voltages. The trade-offs between exposure scaling and dose scaling are likely complicated and beyond the scope of this project, but in general one would likely favor the method that results in lower mean doses to the breast.

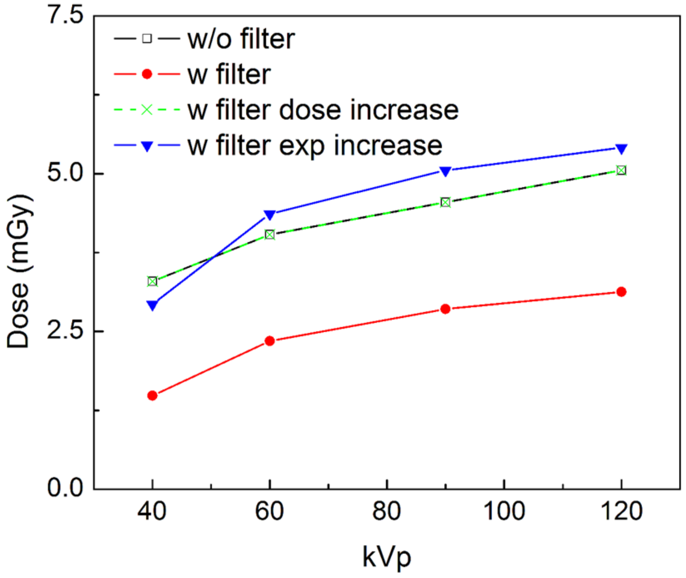

Figure 44. Comparison of measured mean phantom dose versus tube voltage, without adaptive filter, with adaptive filter, and with adaptive filter with either dose-scaled or exposure-scaled increase to tube output.

CHAPTER 4. DISCUSSION

Simulations of the effect of adaptive filtration showed that using an adaptive filter decreased detector count rate to a manageable level, eliminated beam hardening, and improved CNR and CNR uniformity over the image. The average exposure to the breast and to the detector was decreased when the adaptive filter was placed in the beam. For this reason, the average noise in reconstructed CT images was increased compared to images acquired without an adaptive filter. However, x-ray tube output could be increased proportionally such that the average exposure to the breast returns to the same level as without a filter in the beam; such an increase resulted in a corresponding decrease in image noise and increase in CNR. Adaptive filtering with the exposure scaling factor applied eliminated positional dependence of CNR of the contrast elements, and returned the CNR magnitude to similar or higher values than that without adaptive filtration.

The adaptive filter was fabricated from tissue-like material (acrylic) and tested for uniformity of x-ray exposure at the detector surface. If the filter material was different from the material of the breast, then the filter shape optimized for one tube voltage may be suboptimal for other tube voltages due to the different magnitudes of beam hardening associated with different effective atomic numbers of the two materials. Filters based on acrylic, teflon and aluminum were simulated for a 120 kVp tube voltage and beam flatness was assessed at 40 kVp, 60 kVp, and 90 kVp tube voltages to investigate the effect the filters had on the photon count distribution and hardening (Figures 18 and 19). The results in these figures were simulated for 100% glandular breast, which was the worst case scenario for an acrylic filter but a best case scenario for teflon and aluminum filters in reference to effective Z of the phantom material; for breast tissue with 50% glandular and 50% adipose components, the difference of effective atomic numbers of breast and acrylic filter decreased, while the difference between breast and teflon/aluminum increased. The effective atomic numbers of breast with 100% adipose tissue and acrylic were nearly the same, while differences between a breast composed completely of adipose and teflon/aluminum would be the largest. For acrylic filters, x-ray intensity was most non-uniform at 40 kVp (Figure 18a). However, in practice 40 kVp tube voltage would not be optimal for 14 cm diameter breast, and a higher tube voltage would be used. Therefore, one may choose to have filters designed for 50% glandular and 50% adipose breast and use these filters for all breast compositions without having a substantial non-flatness of the beam intensities at the detector surface.

Additionally, an adaptive filter designed for one breast diameter was be suboptimal for other breast diameters. However, multiple adaptive filters to cover a range of breast diameters would be designed to counteract the above issue. Filters for an array of different breast sizes could be easily stacked in a holder for the helical-acquisition fan beam PCS breast CT shown in Figure 6 with either automatic or manual selection for each patient; a similar arrangement would be conceivable for the cone beam breast CT systems under development by other groups as well.

Although adaptive filtration provided substantial advantages for breast CT imaging, including uniformity of CT noise and CNR, decreased beam hardening artifacts, and reduced dynamic range requirements on the detector, its effect on mean breast dose and the spatial distribution of the dose was unknown. The current study performed direct measurements of the spatial distributions and mean values of the breast doses in dedicated breast CT. The dose measurements were performed at tube voltages of 40 kVp, 60 kVp, 90 kVp, and 120 kVp, which were considered useful for breast imaging, with and without an adaptive filter in the beam. The clinically relevant total ESE of 660 mR measured at isocenter was used for all measurements at all tube voltages.

Some interesting and useful effects were observed when mean breast dose and the volume distribution of the dose were compared for breast CT acquired with and without adaptive filtration of the x-ray beam. It was expected that the volume distribution of the breast dose without an adaptive filter should be non-uniform, i.e., a higher dose was deposited to the periphery of the breast than to its central parts because more x-rays are absorbed in the periphery of the breast. This effect was expected at all tube voltages, while its magnitude decreased as tube voltages increased due to higher penetration of the x-rays with increased energy. On the other hand, a more uniform dose distribution was expected when the adaptive filter was used due to the decreased amount of x-rays incident to the periphery of the breast. However, the results reported in Figures 41 and 42 showed that uniformity of the spatial dose distribution with the adaptive filter substantially depended on tube voltage. At tube voltages of 90 and 120 kVp, non-uniformities of the dose distribution with adaptive filtration were as substantial as without the adaptive filter, but the magnitudes of non-uniformities reversed in relative dose distribution. The dose distribution was substantially more uniform for tube voltages of 40 kVp and 60 kVp. It appeared that the adaptive filter over-attenuated the x-ray beam toward the periphery of the phantom in terms of breast dose at 90 kVp and 120 kVp tube voltages, while its attenuation appeared to be near optimal for 40 kVp and 60 kVp tube voltages. However, the adaptive filter was designed and fabricated such that it provided flat intensity of the x-ray beam across the detector surface, which was also tested experimentally. Therefore, an adaptive filter that was optimal for CT image quality at all tube voltages would be suboptimal for dose uniformity at some tube voltages. Figures 27a, 27d, 42a, and 42d show a direct comparison of performance of the adaptive filter and the tradeoffs between CT image noise and dose distribution and the mean values of the dose. The figures include 40 kVp and 120 kVp tube voltages that resulted in the largest magnitude of the dependence of CT noise and dose non-uniformities. It was clear that at tube voltages of 90 kVp and 120 kVp, for a 14 cm diameter breast, the adaptive filter did not provide simultaneously a uniform x-ray intensity at the detector surface and a uniform dose distribution in the breast.

CHAPTER 5. CONCLUSION

Our study has shown that adaptive filtration enables photon counting breast CT through reduction of detector count rate to manageable levels by reducing the signal dynamic range, non-uniformity of beam hardening across the CT image, and CNR non-uniformity as well. These advantages of adaptive filter can also be helpful in current breast CT systems based on conventional energy integrating detectors.

The investigations were performed for all tube voltages potentially useful for breast CT, including 40 kVp, 60 kVp, 90 kVp, and 120 kVp, with and without adaptive filter. The clinically relevant total ESE of 660 mR was used for this study. In the presence of adaptive filter, x-ray tube output was increased to account beam absorption by adaptive filter. Using adaptive filtration eliminated positional dependence of CNR of the contrast elements, and produced similar or higher values of CNR compared to CT scans taken without adaptive filtration.

Our study has also shown that while the breast dose distribution is not uniform without adaptive filter, it may also be non-uniform with adaptive filter at some tube voltages. However, the average dose absorbed in the breast was same with and without adaptive filter.

Consideration must be given in future work to the fact that the filter material may differ in composition from the material of the breast due to the different effective atomic numbers of filter material and breast. Therefore, the filter material should be optimized in future studies to better match for a particular breast composition. Future work should also include design, development, and test of the compound adaptive filter for clinical breast CT systems, and for multiple breast diameters, as well as filters designed for cone beam breast CT systems. The filter placements and breast holder should also be adapted to configurations of the particular breast CT gantries.

LITERATURE CITED

1. Bragg, D.G., P. Rubin, and H. Hricak, *Oncologic Imaging*. 2002, Philadelphia: W.B. Saunders.

2. Harris, J.R., *Diseases of the Breast*. 1996, Philadelphia: Lippincott-Raven Publishers.

3. Glick, S.J., *Breast CT.* Annual Review of Biomedical Engineering, 2007. **9**(1): p. 501 - 26.

4. Karellas, A. and S. Vedantham, *Breast Cancer Imaging: A Perspective for the Next Decade.* Medical Physics, 2008. **35**(11): p. 4878 - 97.

5. Schmidt, T.G., *Dedicated Breast CT: Current Status and New Directions.* Current Medical Imaging Reviews, 2010. **6**(2): p. 61 - 71.

6. Boone, J.M., N. Shah, and T.R. Nelson, *A Comprehensive Analysis of DgNct Coefficients for Pendant-Geometry Cone-beam Breast Computed Tomography.* Medical Physics, 2004. **31**(2): p. 226 - 35.

7. Boone, J.M. and A.L. Kwan, *Computed Tomography for Imaging the Breast.* Journal of Mammary Gland Biology and Neoplasia, 2006. **11**(2): p. 103 - 11.

8. Chen, B. and R. Ning, *Cone-beam Volume CT Breast Imaging: Feasibility Study.* Medical Physics, 2002. **29**(5): p. 755 - 70.

9. Bushberg, J.T., *The Essential Physics of Medical Imaging*. 2002, Philadelphia: Lippincott Williams.
10. Boone, J.M. and T.R. Nelson, *Dedicated Breast CT: Radiation Dose and Image Quality Evaluation.* Radiology, 2001. **221**(3): p. 657 - 67.

11. Shikhaliev, P.M., *Computed Tomography with Energy-resolved Detection: A Feasibility Study.* Physics in Medicine and Biology, 2008. **53**(5): p. 1475 - 95.

12. Boone, J.M., et al., *Technique Factors and Their Relationship to Radiation Dose in Pendant Geometry Breast CT.* Medical Physics, 2005. **32**(12): p. 3767 - 76.

13. Saslow, D., et al., *American Cancer Society Guidelines for Breast Screening with MRI as an Adjunct to Mammography.* Cancer, 2007. **57**(2): p. 75 - 89.

14. Bassett, L.W., *Quality Determinants of Mammography*, D.o.H.a.H. Services, Editor 1994, Public Health Service: Rockville, MD.

15. Hounsfield, G.N., *Computerized Transverse Axial Scanning (Tomography): Part 1. Description of System.* British Journal of Radiology, 1973. **46**(552): p. 1016 - 22.

16. Chang, C.H., *Computed Tomography of the Breast.* Radiology, 1977. **124**(3): p. 827 - 29.

17. Chang, C.H., et al., *Computed Tomography in Detection and Diagnosis of Breast Cancer.* Cancer, 1980. **46**(S4): p. 939 - 46.

18. Kwan, A.L., J.M. Boone, and N. Shah, *Evaluation of X-ray Scatter Properties in a Dedicated Cone-beam Breast CT Scanner.* Medical Physics, 2005. **32**(9).

19. Liu, B., S.J. Glick, and C. Groiselle, *Characterization of Scatter Radiation in Cone Beam CT Mammography.* SPIE Phys. Med. Imag., 2005: p. 5745:818-27.

20. Bhagtani, R. and T.G. Schmidt, *Simulated Scatter Performance of an Inverse-geometry Dedicated Breast CT System.* Medical Physics, 2009. **36**(3): p. 788-96.

21. Siewerdsen, J.H., et al., *The Influence of Antiscatter Grids on Soft-tissue Detectability in Cone-beam Computed Tomography with Flat-panel Detectors.* Medical Physics, 2004. **31**(12).

22. Beutel, J. and H.L. Kundel, *Handbook of Medical Imaging*. 2000, Bellingham, WA: SPIE Press.

23. Glick, S.J., et al., *Evaluating the Impact of X-ray Spectral Shape on Image Quality in Flat-panel CT Breast Imaging.* Medical Physics, 2007. **34**(1): p. 5-24.

24. Barber, W.C.e.a., *Characterization of a novewl photon counting detector for clinical CT: count rate, energy resolution, and noise performance.* Proc. SPIE, 2009. **7258**: p. 2401 - 9.

25. Bornefalk, H. and M. Danielsson, *Photon-counting spectral computed tomography using silicon strip detectors: a feasibility study.* Physics in Medicine and Biology, 2010. **55**: p. 1999 - 2022.

26. Cajipe, V.B.e.a., *Multi-energy x-ray imaging with linear CZT pixel arrays and integrated electronics.* Nuclear Science Symposium Conference Record, 2004 IEEE, 2004. **7**: p. 4548 - 51.

27. Iwanczyk, J.S.e.a., *Photon counting energy dispersive detector arrays for x-ray imaging.* Nuclear Science Symposium Conference Record, 2007 IEEE, 2007: p. 2741 - 8.

28. Schmidt, T.G., *Optimal 'image-based' weighting for energy-resolved CT.* Medical Physics, 2009. **36**: p. 3018 - 27.

29. Shikhaliev, P.M., *Beam Hardening Artefacts in Computed Tomography with Photon Counting, Charge Integrating and Energy Weighting Detectors: A Simulation Study.* Physics in Medicine and Biology, 2005. **50**(24): p. 5813 - 27.

30. Shikhaliev, P.M., *The Upper Limits of the SNR in Radiography and CT with Polyenergetic X-rays.* Physics in Medicine and Biology, 2010. **55**: p. 5317 - 39.

31. Frey, E.C.e.a., *Micro computed tomography with a photon-counting x-ray detector.* Proc. SPIE, 2007. **6510**: p. 65101R-1-6.

32. Shikhaliev, P.M., *Projection X-ray Imaging with Photon Energy Weighting: Experimental Evaluation with a Prototype Detector.* Physics in Medicine and Biology, 2009. **54**(16): p. 4971 - 92.

33. Taguchi, K.e.a., *An analytical model of the effects of pulse pileup on the energy spectrum recorded by energy energy resolved photon counting x-ray detectors.* Medical Physics, 2010. **37**(3957 - 69).

34. Le, H.Q. and M. S., *Least squares parameter estimation methods for material decomposition with energy discriminating detectors.* Medical Physics, 2011. **38**: p. 245 - 55.

35. Roessl, E. and R. Proksa, *K-edge imaging in x-ray computed tomography using multi-bin photon counting detectors.* Physics in Medicine and Biology, 2007. **52**: p. 4679 - 96.

36. Shikhaliev, P.M., *Energy-resolved Computed Tomography: First Experimental Results.* Physics in Medicine and Biology, 2008. **53**(20): p. 5595 - 613.

37. Wang, A. and N.J. Pelc, *Optimal energy thresholds and weights for separating materials using photon counting x-ray detectors with energy discriminating capabilities.* Proc. SPIE, 2009. **7258**: p. 2101 - 12.

38. Wang, A. and N.J. Pelc, *Sufficient statistics as a generalization of binning in spectral x-ray imaging* IEEE Transactions on Medical Imaging, 2010. **30**: p. 84 - 93.

39. Bornefalk, H. and M. Lundqvist, *Dual-energy imaging using a photon counting detector with electron spectrum-splitting.* Proc. SPIE, 2006. **6142**: p. 1H-1-11.

40. Bornefalk, H., H. M., and H. T., *Contrast-enhanced dual-energy mammography using a scanned multi-slit system: evaluation of a differential beam filtering technique.* Journal of Electronic Imaging, 2007. **16**(2): p. 023006.

41. Schlomka, J.P.e.a., *Experimental feasibility of multi-energy photon counting K-edge imaging in pre-clinical computed tomography.* Physics in Medicine and Biology, 2008. **53**: p. 4031 - 47.

42. Shikhaliev, P.M., *Photon Counting Spectral CT Versus Conventional CT: Comparative Evaluation for Breast Imaging Application.* Physics in Medicine and Biology, 2011. **56**: p. 1905 - 30.

43. Shikhaliev, P.M., *Photon Counting Spectral CT: Improved Material Decomposition with K-edge Filtered X-rays.* Physics in Medicine and Biology, 2012. **57**: p. 1595 - 1615.

44. Kalender, W.A., et al., *High-resolution spiral CT of the breast at very low dose: concept and feasibility*. European Journal of Radiology, 2012. **22**: p. 1 - 8.

45. Silkwood, J.D., K.L. Matthews, and P.M. Shikhaliev, *Photon Counting Spectral Breast CT: Effect of Adaptive Filtration on CT Numbers, CT Noise, and CNR.* Submitted to Medical Physics, 2013.

46. Silkwood, J.D., K.L. Matthews, and P.M. Shikhaliev, *Dedicated Breast CT: Effect of Adaptive Filtration on Breast Dose.* Submitted to Medical Physics, 2013.

47. Chang, C.H.e.a., *Specific Value of Computed Tomographic Breast Scanner (CT/M) in Diagnosis of Breast Diseases.* Radiology, 1979. **132**: p. 647 - 52.

48. Karellas, A., J.Y. Lo, and C.G. Orton, *Cone Beam X-ray CT Will Be Superior to Digital X-ray Tomosynthesis in Imaging the Breast and Delineating Cancer.* Medical Physics, 2008. **35**(2): p. 409 - 11.

49. Ning, R., *A Novel Cone Beam Breast CT Scanner: System Evaluation.* Proc. SPIE, 2007. **6510**: p. 301 - 9.

50. Brooks, R.A. and G.D. Chiro, *Statistical Limitations in X-ray Reconstructive Tomography.* Medical Physics, 1976. **3**(4): p. 237 - 240.

51. Kalender, W.A., *Computed Tomography*. 2006, Munich: Publicis MCD Verlag.

52. Poludniowski, G., et al., *SpekCalc: A Program to Calculate Photon Spectra from Tungsten Anode X-ray Tubes.* Physics in Medicine and Biology, 2009. **54**(19): p. 433-38.

53. Hubbell, J.H. and S.M. Seltzer, *Tables of X-ray Mass Attenuation Coefficient and Mass Energy Absorption Coefficients 1 keV to 20 MeV for elements Z = 1 to 92 and 48 Additional Substances of Dosimetric Interest*. 1995, NIST: Gaithersburg. p. 111.

54. XCOM, N., http://www.nist.gov/pml/data/xcom/index.cfm, 2013.

55. MATLAB, version 7.5.0.342. Natick, Massachusetts: The MathWorks Inc., August 15, 2007.

56. Rasband, W., ImageJ 1.46r National Institutes of Health, USA, 2012.

57. Shikhaliev, P.M., *Tilted Angle CZT Detector for Photon Counting/energy Weighting x-ray and CT Imaging.* Physics in Medicine and Biology, 2006. **51**(17): p. 4267 - 87.

58. Schlomka, J.P., et al., *Experimental Feasibility of Multi-energy Photon-counting K-edge Imaging in Pre-clinical Computed Tomography.* Physics in Medicine and Biology, 2008. **53**(15): p. 4031 - 47.

59. Russo, P., T. Coppola, and G. Mettivier, *Distribution of Absorbed Dose in Cone-beam Breast Computed Tomography: A Phantom Study with Radiochromic Films.* IEEE Transactions on Nuclear Science, 2010. **57**(4): p. 2220 - 9.

60. Sechopoulos, I., S.J. Feng, and C.J. D'Orsi, *Dosimetric Characterization of a Dedicated Breast Computed Tomography Clinical Prototype.* Medical Physics, 2010. **37**(8): p. 4110 - 20.

61. Thacker, S.C. and S.J. Glick, *Normalized Glandular Dose (DgN) Coefficients for Flat-panel CT Breast Imaging.* Physics in Medicine and Biology, 2004. **49**(24): p. 5433 - 44.

APPENDIX A.

A.1. Gantry design with fan beam geometry and helical motion

CT has advanced through multiple generations since its beginnings in the early 1970s. Currently, the most popular CT gantry design incorporates a rotating tube and detector array along a helical trajectory about the patient. To accomplish this, the patient was translated through the CT scanner on a table at a uniform rate as the tube and detector array rotated about the patient. The two most popular beam geometries historically used in CT scanning were parallel beam and fan beam geometry, shown in Figure 45.

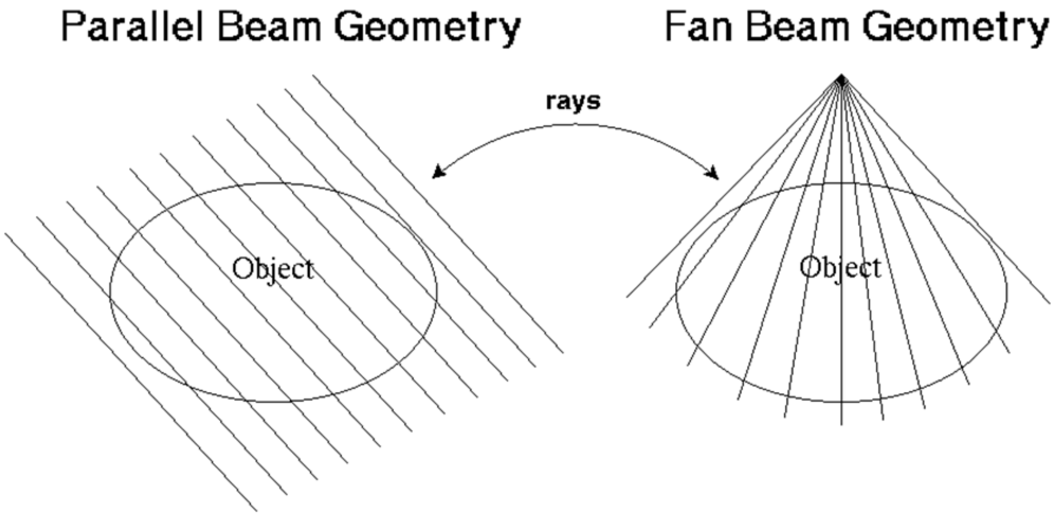

Figure 45. Comparison of parallel and fan beam geometry as used in CT acquisition.

Parallel beam geometry was used in the earliest CT systems. A point-like x-ray beam, known as a pencil beam, obtained measurements by first translating across the patient with the detector opposite, and then the gantry rotated slightly before the pencil beam translated across the patient again. Scans took a relatively long time for these early CT scanners. Fan beam scanning emerged as a way to speed up scanning times. These scanners produced a beam that was thin, but wide enough to encompass the entire patient's width in the beam. This eliminated the need to translate the tube across the patient; however, rotation of the tube and detector about the patient was still necessary. Appendix section A2 gives an explanation as to why rotation is necessary for CT scanning. The combination of rotating gantry and translation of the patient on the couch through the bore produced a helical acquisition of data.

A.2. Measuring total attenuation and reconstruction

CT scanning in its most basic form is a measurement of the spatial distribution of attenuation within the object, based on a certain number of projections of total attenuation. An example is shown in Figure 46.

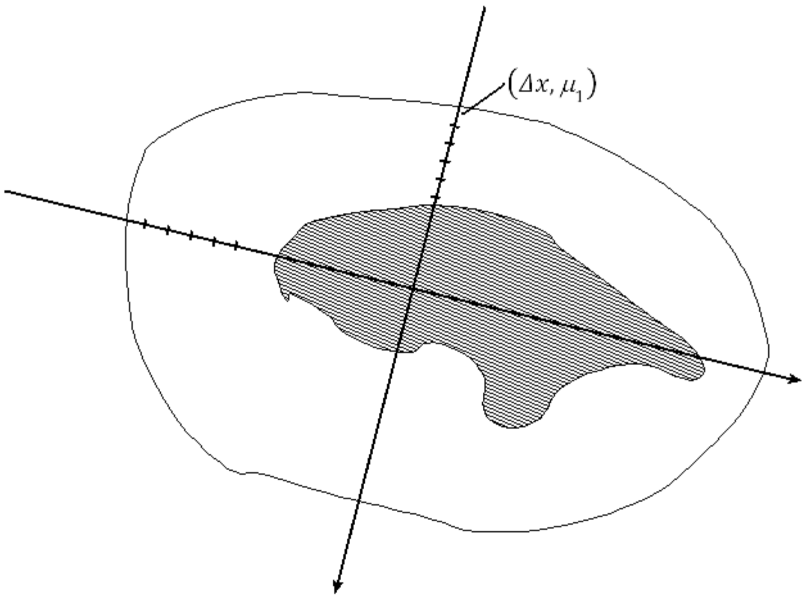

$$\text{line integral} = \Delta x \sum \mu_i = \int_0^L \mu(x)\mathrm{d}x$$

Figure 46. Two projection lines through a breast are shown with two tissue types: adipose on the exterior and glandular on the interior. The projection value is determined from the sum of the attenuation coefficients over each distance Δx.

This simple analogy of CT scanning shows 2 projection lines approximately perpendicular to each other. An attenuation coefficient μ_i is determined in steps of Δx. The sum of μ_i over the object's total attenuation path length L yields the sinogram value for that particular projection and path. This method is known as forward projection.

A method called backprojection was used to reconstruct CT images. Backprojection was subdivided into two main types: simple and filtered backprojection. Simple backprojection first took each projection recording and smeared the pixel values back along the acquisition angle over the image matrix. The backprojections were then summed together yielding a final image matrix. Performing backprojection in this manner, however, did not produce an accurate final image. This was due to 1/r blurring, where r is the radius from the center of rotation of the scanner.

Filtered backprojection emerged as a way to undo the blurring found in simple backprojection by convolving a convolution kernel with the simple backprojection data. The end result was an image of the object with minimal artifacts due to reconstruction.

A.3. Beam hardening and cupping artifact

The HVL of an x-ray beam is defined as the thickness necessary of a particular object to cut the beam intensity to half of its original value. HVLs may be specified using any material, but typically it's specified in terms of mm aluminum. X-ray beams used in clinical CT are polyenergetic, with typical energies ranging from 25 keV to 120 keV. When a polyenergetic spectrum is passed through an attenuating material, the lower energy components of the beam are preferentially screened out. This screening out of low energy photons makes each subsequent HVL longer than the previous. This process is referred to as Beam Hardening. Beam hardening occurs because the lower energy portion of the spectrum has a higher likelihood of interacting with the material it’s passing through. This likelihood of interaction can be quantized as attenuation coefficients.

Every unique type of matter possesses a range of energy dependent attenuation coefficients. The National Institute of Standards and Technology has an online database called XCOM that lists the attenuation coefficients for hundreds of materials over a practical energy range for use in Medical Physics. When in pendant position, breast tissue presents a circular cross-section with varying thickness across its profile. Whether the x-ray beam passes through the periphery or center of the breast determines the total attenuation length in its path. The end result of a CT scan is an image of cylindrical object, with HU values (defined in section 2.3.2) highest along the periphery, and lowest at the center. This occurs because the rays that pass through the periphery of the breast have less attenuating material to travel through, and more low energy photons arrive at the detector surface. This is defined as a cupping artifact; so called because of the cup-like shape of a cross-sectional profile of the object in terms of HU.

A.4. Effect of filtration

X-ray spectra for this work have been defined using two parameters: HVL (defined earlier), and kVp. HVL is a measure of beam quality, while kVp is the highest energy present in the x-ray beam. Characteristic x-rays did not begin to appear until photon energy surpassed 69 keV, the k-edge of tungsten. Shown in Figure 48 are two x-ray spectra: one below the k-edge of tungsten, and one above the k-edge of tungsten. Below the k-edge, the only photons produced are called bremsstrahlung photons, or breaking photons, which were the byproduct of electrons interacting with tungsten nuclei in the anode. Figure 48(a) shows an x-ray spectra comprised of bremsstrahlung photons only. Beyond the k-edge, characteristic photons were produced, which were photons produced from tungsten electrons cascading down to lower energy state holes. These holes were created by photoelectric interactions with tungsten electrons. The characteristic photons presented as spikes in the spectra shown in Figure 48(b). Before exiting the x-ray tube, the beam is passed through a filter to absorb low energy photons that would have raised patient dose without contributing to the diagnostic quality of the beam.

A.5. Contrast to noise ratio

Contrast to noise ratio (CNR) is defined as CNR = (S – B)/σ, where S is the signal of the object of interest, B is the signal of the background material, and σ is the magnitude of the noise in the image. A large component of this work was devoted to maximizing the CNR, because a higher CNR corresponds to a more viewable object.

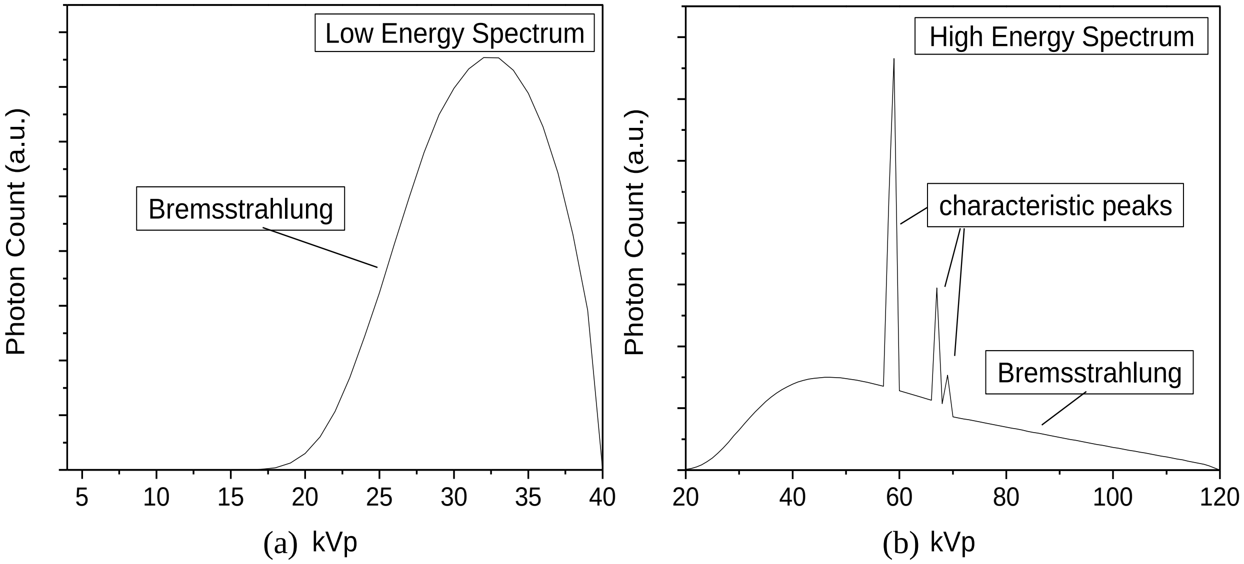

(a)

(b)

Figure 47. Two spectra are shown. The low energy spectrum (a) did not contain any characteristic photons because it did not possess photons with enough energy to liberate k-shell electrons. The high energy spectrum (b) contains both characteristic and bremsstrahlung photons, as a portion of the beam possessed enough energy to produce characteristic x-rays.

APPENDIX B.

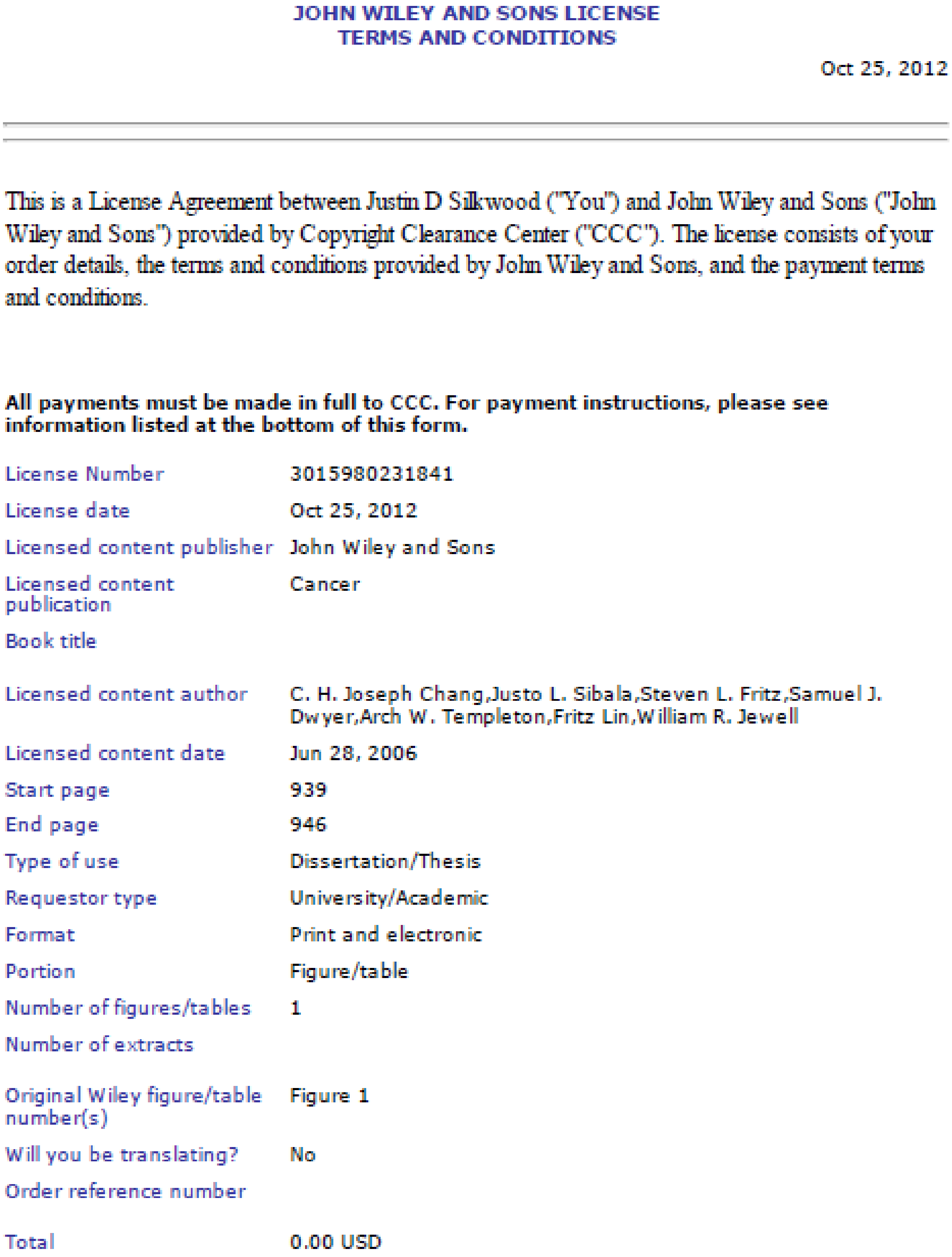

JOHN WILEY AND SONS LICENSE
TERMS AND CONDITIONS

Oct 25, 2012

This is a License Agreement between Justin D Silkwood ("You") and John Wiley and Sons ("John Wiley and Sons") provided by Copyright Clearance Center ("CCC"). The license consists of your order details, the terms and conditions provided by John Wiley and Sons, and the payment terms and conditions.

All payments must be made in full to CCC. For payment instructions, please see information listed at the bottom of this form.

License Number	3015980231841
License date	Oct 25, 2012
Licensed content publisher	John Wiley and Sons
Licensed content publication	Cancer
Book title	
Licensed content author	C. H. Joseph Chang,Justo L. Sibala,Steven L. Fritz,Samuel J. Dwyer,Arch W. Templeton,Fritz Lin,William R. Jewell
Licensed content date	Jun 28, 2006
Start page	939
End page	946
Type of use	Dissertation/Thesis
Requestor type	University/Academic
Format	Print and electronic
Portion	Figure/table
Number of figures/tables	1
Number of extracts	
Original Wiley figure/table number(s)	Figure 1
Will you be translating?	No
Order reference number	
Total	0.00 USD

VITA

Justin Silkwood was born in Midwest City, Oklahoma, in January 1987. He is the son of Ed and Kimberly Silkwood. He graduated from Norman High School in 2005, and went on to major in Engineering Physics and Mathematics at Southwestern Oklahoma State University in Weatherford, Oklahoma. Upon receiving his degree in May, 2010, Justin enrolled at Louisiana State University at Baton Rouge to study Medical Physics, where he became a candidate for the master of science degree in medical physics.